“Calculation of the Effective Atomic Number for the Iodine Contrast Agent of the Varying Concentrations”

Olga V. Pen

Thesis submitted to the faculty of the Virginia Polytechnic Institute and State University in partial fulfillment of the requirements for the degree of

Master of Science

In

Biomedical Engineering

Chair: Guohua Cao

John D. Bourland

Steven M. LaConte

July, 25, 2016

Blacksburg, VA, USA

Keywords: x-ray imaging, color CT, effective atomic number, iodine contrast agent

“Calculation of the Effective Atomic Number for the Iodine Contrast Agent of the Varying Concentrations”

Olga V. Pen

ABSTRACT

The author discusses the difficulties that arise with the determination of the concentration of the iodinated contrast agents in the blood stream via the traditional gray-scale computer tomography and searches for the new imaging modalities that would provide for better sensitivity. The topic of the energy-discriminative color CT is discussed as a potential solution and its suitability is evaluated by performing the experiments on the contrast materials phantom and the phantom containing the iohexol solutions of varying concentrations on the original CT system assembled by the author. A method of the effective atomic number mapping is discussed as a viable alternative to the traditional attenuation-based tomography. The dependency of the effective atomic number of the compound on the energy of the x-ray beam is a phenomenon well recorded in the literature, yet no formal study exists to correctly predict the effective atomic number for a given compound. An extensive physical model is developed based on the previously presented models and adaptations unique to the task in order to determine the effective atomic numbers for exact energies experimentally. The method is tested on different materials. The resultant effective atomic numbers for the water, oil, and iohexol-water solutions of varying concentrations are presented in the study. The effects of the k-edge on both the linear attenuation curve and the effective atomic number curve are discussed. The possible future venues of the research are presented in the final part of the thesis.

Table of Contents

INTRODUCTION

The administration of the iodine contrast agent is a vital step in the modern diagnostic radiology. Ever since 1950's, it has found wide use in the medical practice. It is particularly effective in enhancing the visibility of the vasculature and organs and it employed for the cancer diagnostics, blood pool imaging, cardiac imaging, kidney imaging, as well as other possible applications. Iodine based contrast agent is well-suited for the contrast enhancement and at the same time possesses relatively low toxicity, allowing for its wide clinical use. Depending on the size of iodine-containing molecules and particles in the iodine solution, as well as possible coating, the circulation time of the iodine contrast agent can last from minutes to hours, allowing for the thorough CT scan without creating the necessity for numerous injection [1]. Current advances in the iodine nanoparticles production allow to introduce the particular tissue-attractive coating to the iodine-containing nanoparticles, which in turn allows for the targeting for the specific organs, tissues and cell types, such as breast tumor [2], lung cancer [3], or specific affected macrophages in the atherosclerotic plaques [4].

While a wide variety of the iodine-based contrast agents exist, the iodinated contrast agent (ICA) solutions are by far the most commonly used. The estimated yearly use of the ICA reaches approximately 75 million doses worldwide [5], with the number constantly increasing. The ICA can be subdivided into four main categories depending on the chemical composition variation, each possessing unique physical and biological properties. All ICA share the same basic function group – tri-iodinated benzene ring. The size of the covalently bonded iodine atom (133 picometers) falls within the range of the wavelength of the x-ray (10-10000 picometers), thus ensuring the relatively high x-ray attenuation by the iodine [6]. The benzene ring provides the stable construct of the three iodine atoms in relative proximity, both increasing the effective molecular size

(which causes the attenuation of the longer wavelength x-rays) and reducing the toxicity [7]. The four types of the ICA include ionic monomer, ionic dimer, nonionic monomer and nonionic dimer. In this particular work, the nonionic monomer group has been extensively investigated. The 1-N,3-N-bis(2,3-dihydroxypropyl)-5-[N-(2,3-dihydroxypropyl)acetamido]-2,4,6-triiodobenzene-1,3-dicarboxamide, also known as iohexol contrast agent, sold under the commercial names "Omnipaque" and "Exypaque", is actively used in the clinical practice. Iohexol chemical formula is $C_{19}H_{26}I_3N_3O_9$, with its molar mass being 821.138 g/mol. The iohexol solution used in this particular work was "Omnipaque 350", indicating the concentration of 350 mg of pure iodine per ml of the solution. The skeletal formula for iohexol is presented on the figure below:

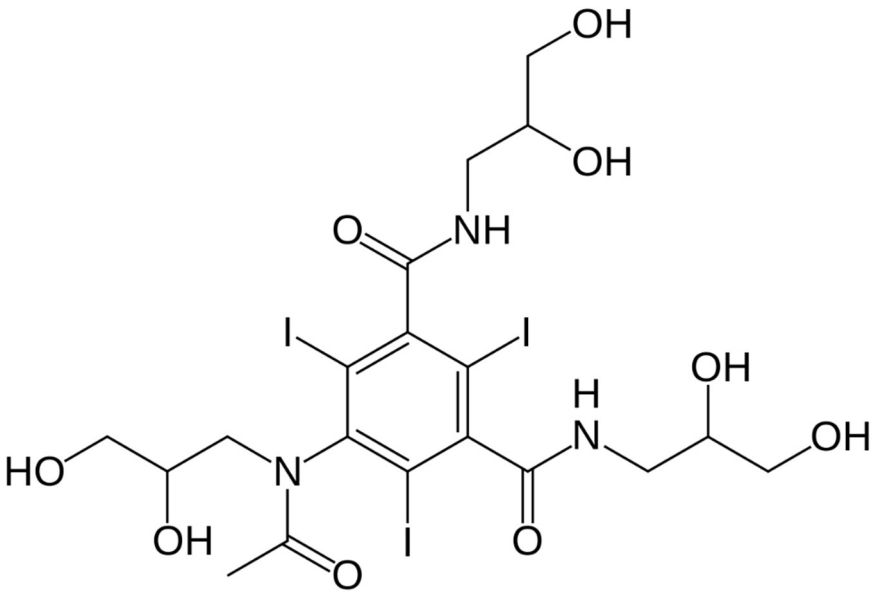

Figure 1 – Iohexol chemical formula

The particular concentration of the iodine in the "Omnipaque 350" solution has been long established by the clinical trials and medical practice as optimal for the imaging purposes, as it provides the adequate contrast while maintaining relatively low toxicity levels. However, the efforts to decrease the necessary concentration of the iodine in the solution while maintaining the image quality remain a venue of research.

Possible adverse reactions to the iodine contrast agent include nausea, vomiting, hemodynamic changes, bradycardia, hypotension, arrhythmia, rash, angioedema, bronchospasm, cardiovascular collapse [7]. A particular concern is contrast-induced nephropathy that has been known to be directly linked with the high volume of contrast agent and high concentrations of iodine in particular. Thus, the search for the alternative imaging modalities and image processing techniques that would allow lowering the concentration of iodine in the solution while providing the accurate way to detect iodine is imperative.

On the other hand, the detection of variation of the iodine concentration with contrast agent already injected also remains a problem that could significantly increase the accuracy of the diagnoses in the cases of the blood pool imaging, as well as the targeted iodine-based nanoparticle contrast agent solutions that would be attracted to the particular type of tissue of cells. Unfortunately, in the conventional CT, the differentiation between the different concentrations of iodine in the tissue remains a problem. Several studies has been performed in order to establish the variation in response for the different concentrations of iodine [8][9][10][11][12]. However, the aforementioned research still indicates the necessity for the high percent of the pure iodine in the ICA solutions in order to provide the sufficient contrast in the traditional attenuation-based CT. Thus, the attempt has been made to research the alternative imaging modalities.

One of such methods lies in the effective atomic number mapping. The effective atomic number is the average atomic number of the compound or mixture that is calculated as the combination of the respective atomic numbers of the elements that comprise the mixture. It is useful in understanding the relative strength of the binding energy for the electrons on different orbitals, thus contributing to the effective nuclear charge. However, for the purposes of the diagnostic CT, a much more important aspect of the effective atomic number is its ability to describe the nature of the material or

compound interaction with the radiation. The cross-sections for the photoelectric absorption, as well as coherent and incoherent scattering occurring due to Compton and Rayleigh effects, are all dependent of the effective atomic numbers of the irradiated material. Various methods have been proposed in order to find the effective atomic numbers of the compound. Three major methods described in the literature are [13]:

1) Mass-weighted average
2) Power-law type method with a crude approximation of the relationships between the interacting cross-sections
3) Direct calculations of the interacting cross-sections for each particular scenario, most of the time based on the experimentally obtained measurements.

The first method has not been very accurate in predicting the material's interaction with the matter and as thus has not been widely utilized. The second approach has found application that is much more widespread in the scientific community. Generally, the power law method of calculating the effective atomic number of the compound can be summarized as:

$$Z_{eff} = \sqrt[n]{\sum_{i=1}^{k} Z_i^n f_i} \quad (1)$$

Where Z_{eff} is the effective atomic number of the compound, Z_i is the i-th element that constituents the compound, f_i is the fractional weight of the i-th element in the compound overall molecular weight, k is the number of elements in the compound, and n is the power parameter that depends on the nature of major radiation interaction mode occurring at the particular energy. The exponent value n has a variety of values, ranging from $n = 1$ for the Compton effect, $n = 4$ to 5 for the photoelectric effect and $n = 2$ for the pair production [14]. For the transient regions where no certain dominant effect could be established, the values range from $n = 2.94$ [15], to $n = 3.1$ [16], to $n = 4$ [17] for the diagnostic x-ray range. The dependency of the effective atomic number on the

exact relationship between the cross-sections for the varying effects make the effective atomic number of the compounds strongly dependent on the energy range of the x-ray beam. The lack of the precise energy boundaries that would make application of the particular exponential power value more clear for the particular scanning protocol make it difficult to determine the exact effective atomic number of the particular compound. However, the aforementioned method can still be used in order to calculate the approximate value of the effective atomic number. Therefore, formula (1) can be applied to calculate the approximate atomic number of the iohexol as described by the chemical formula given in figure 1.

The third method for calculating the effective atomic number relies on the estimation of the cross-sections for each major type of interactions of the x-ray photons with the medium electrons, namely, photoelectric, coherent scattering and incoherent scattering. Several models have been proposed that are capable of calculating the effective atomic number for the known compound for a chosen energy. The majority of these models utilize the measurements of the mass or linear attenuation coefficients for the material, which can be obtained by performing the regular CT scan. For the photoelectric effect, if the medium material or compound has been known beforehand, then simple formula can be applied in order to estimate the atomic cross-section [18][19].

$$\sigma_i = \frac{A_i}{N_A}\left(\frac{\mu}{\rho}\right) \quad (2)$$

Where A_i is the atomic weight, N_A is the Avogadro's number, $\frac{\mu}{\rho}$ is the mass attenuation coefficient, and σ_i is the atomic cross-section for a particular material in the mixture. In this case the effective atomic number can be found as:

$$Z_{eff} = \frac{\sum_i f_i A_i (\frac{\mu}{\rho})_i}{\sum_j f_j \frac{A_j}{Z_j} (\frac{\mu}{\rho})_j} \quad (3)$$

Where f_i is the fractional weight of the particular element in the compound.

For the Compton Effect, however, the atomic cross-section is expressed as:

$\sigma_{C,i} = Z_i \sigma_0$ (4)

Where σ_0 is constant and the effective atomic number can be found as:

$Z_{eff} = \frac{1}{n} \sum_i n_i Z_i = \sum_i f_i Z_i$ (5)

Thus, for the Compton scattering the effective atomic number is equal to the mean atomic number. Analogous expression is applied for the coherent scattering.

The effective atomic number combined for all three types of interaction is calculated by applying the weighting factor for the effective atomic number obtained for each type of interaction. The weighting factors are calculated as the ratio of the interaction cross-section of a particular type to the total cross-section for the chosen element or compound, as is calculated in accordance with the NIST database. The method has been automated by the program crated by Taylor et al. [19], with numerous examples demonstrating the truthfulness of the model [18][19]. However, the aforementioned model is only applicable once the compound is already known, and thus, is of limited practical application.

More complex models are required for the case where the compound is unknown and only linear attenuation coefficient measurement is available. In this case, a single measurement is not enough to provide enough information in order to determine the effective atomic number. The dual-energy measurements CT are used instead. The idea to apply the dual-energy CT for the purposes of identifying the effective atomic numbers was first presented by Hounsefield in 1973 [20]. Since then, it has found further development and refinement. Two separate issues arise while trying to determine the effective atomic number via dual-energy CT. First one is the selection of the model. A great variety of models that transform the linear attenuation measurements

for the two energies to a single atomic number exist. Some of them rely on the adjustable proportionality coefficient that directly links the effective atomic number to the measured linear attenuation coefficients. The proportionality coefficient can be established empirically [21] [22], or through an algebraic optimization procedure [23]. On the other hand, physics-based models link the measured linear attenuation coefficient and the corresponding effective atomic number via the complex relationship described by the cross-section parametrization formulas that take into account the physical effects of x-ray photon interaction with the medium electrons[24][25][26]. The later will be examined in this particular work. The detailed description of the model and the physical phenomena underlying it can be found in the following chapters.

The dual-energy CT utilized in the aforementioned works is based on the two measurements obtained for either two separate measurements taken for a single source-detector pair, with the source switching between two peak energies, or for two pairs or sources-detectors operating simultaneously. While this method allows for the acquisition of the two distinct attenuation coefficients, a major disadvantage of the dual-energy CT lies in the necessity to deposit a double amount of dose to the patient in order to obtain two readings. In the clinical setting with the prevalent ALARA principal, the benefits of the dual-energy CT often do not outweigh the risks of the additional irradiation, making the proposed method ill suited for the practical application. However, the recent emergence of the energy-discriminative color CT detectors proposes an alternative solution. The energy discriminative detector allows recording the number of photons that possess a particular energy, thus eliminating the necessity to operate the x-ray tube at two distinct peak energies. Instead, the energy spectrum naturally generated by the polychromatic x-ray source provides enough photons of the varying energies that the attenuation coefficients for the photons at the particular chosen energy bins can be reconstructed from a single reading. This simultaneously reduces the dose, the scanning time, and allows for the acquisition of the information necessary

in order to determine the effective atomic number in the fashion similar the processing of the attenuation map obtained via the traditional dual-energy CT scan performed with the help of the energy integrating detectors.

The schematics of the energy discriminative detector are presented below:

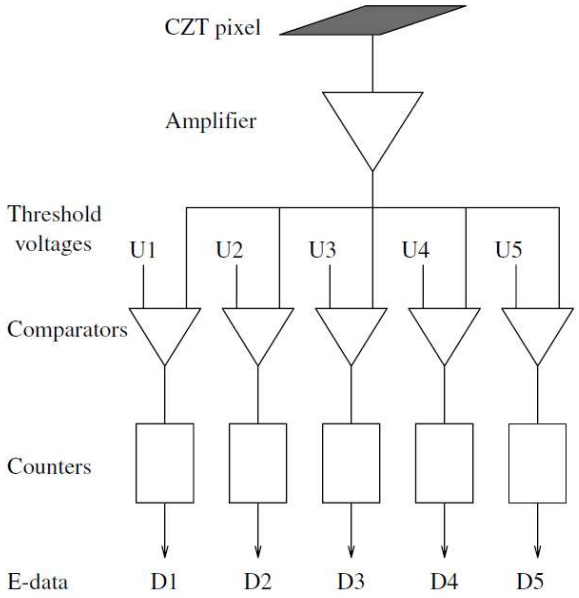

Figure 2 – Energy discriminative detector schematics

As can be seen from the figure 2, the thresholds for each energy bin set the borderline voltage, and the comparators serve for the bin differentiation, determining whether the photon energy passed a certain threshold. The overall spectrum is then subdivided, as presented on the figure 3:

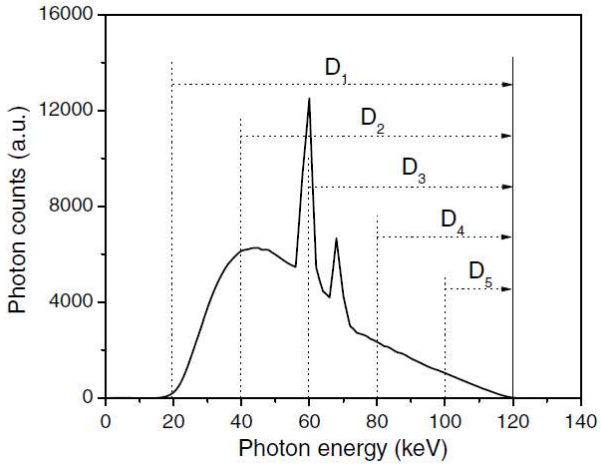

Figure 3 – Energy spectrum divided into six bins. Each pixel OUTPUT has 5 discrete numbers corresponding to D_1, D_2, …, D_5

Here we can see that each D_i represents the number of photons with the energy higher than a certain E_i, and the number of photons in each energy bin can be found as $D_i - D_{i-1}$.

The advantages of the color CT energy-discriminative imaging in comparison to the traditional energy-integrative imaging will be illustrated later on in this work. In the proposed work, multiple measurements are taken within a single scan, with the overall number of measurements for the same energy spectrum varying from 6 (various materials contrast phantom) to 9 (phantom with the iodine contrast agent filling of the varying concentration). This allows to calculate the effective atomic number that characterizes the whole spectrum by incorporating all measurements within a single system of equations, as well as measure the variation of the effective atomic number from energy to energy within a range of energies in the spectrum. Based on that, important material properties can be derived.

MATERIALS AND METHODS

Physical model

In the modern x-ray computer tomography, the imaged object is placed under the x-ray beam of the known initial intensity (I_0) that is attenuated in the process, resulting in the signal weakened in comparison to I_0 being registered on the detector. The relationship between the two signal can be described by Lambert-Beer's law [27]:

$$\frac{I}{I_0} = \exp(-\mu x) \quad (6)$$

Where μ represents the attenuation coefficient of the encountered matter and x corresponds to the x-ray's path in geometrical terms. The attenuation coefficients are unique to the particular materials, compound and mixtures, and are closely correlated to the effective atomic numbers and electron densities of the material via their dependency on the differential cross-sections that result from the x-ray photon interaction with the matter. In the diagnostic x-ray range (20-150 keV) the majority of interactions between x-ray photons and the electrons of the material in question can be divided into three categories: coherent scattering, incoherent scattering, and photoelectric effect. Thus, the linear attenuation coefficient of the materials can be presented as [28]:

$$\mu(E, Z, \rho_e) = \rho_e * \left[{}_e\sigma^{coh}(E, Z) + {}_e\sigma^{incoh}(E, Z) + {}_e\sigma^{ph}(E, Z) \right] \quad (7)$$

Where ρ_e is the electron density of the material, E corresponds to the energy of the x-ray beam, Z corresponds to the effective atomic number of the material, ${}_e\sigma^{co}(E, Z)$ corresponds to the coherent scattering differential cross-section, ${}_e\sigma^{incoh}(E, Z)$ corresponds to the incoherent scattering cross-section, and

${}_e\sigma^{ph}(E,Z)$ corresponds to the photoelectric cross-section. Electron density itself can be calculated as [26]:

$$\rho_e = \frac{\rho N_A}{A} * Z \quad (8)$$

Where ρ corresponds to the volumetric mass density, N_A corresponds to the Avogadro's number, A is atomic mass. Formula (2) can be re-written as:

$$\mu(Z,E,\rho_e) = \rho_e[Z^4 * F(Z,E) + G(Z,E)] \quad (9)$$

Where $F(Z,E)$ corresponds to the photoelectric cross-section, and $G(Z,E)$ corresponds to the combined coherent and incoherent scattering cross-sections. If two separate attenuation coefficients measured at two distinct energies are available, the effective atomic number can then be calculated as:

$$Z^4 = \frac{\mu(E_2)G(E_1,Z) - \mu(E_1)G(E_2,Z)}{\mu(E_1)F(E_2,Z) - \mu(E_2)F(E_1,Z)} \quad (10)$$

Which can be solved iteratively.

The derivation of the terms $F(Z,E)$ and $G(Z,E)$ is provided below.

Parametrization for the photoelectric effect.

Photoelectric effect, or photoelectric absorption, is a process in which the x-ray photon hits the target electron and is absorbed, completely transferring its energy to the electron. This electron (photoelectron) is then emitted. The effects of the photoelectric effect can be presented by the following graph:

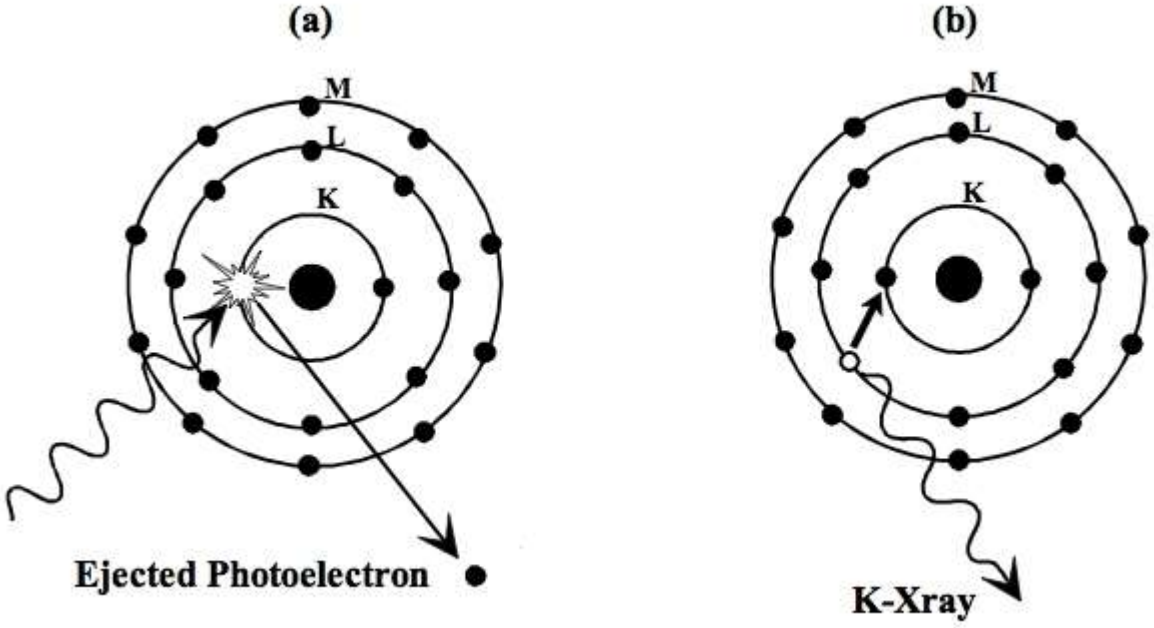

Figure 4 - Photoelectric effect resulting in a) absorption of the incoming x-ray photon and emission of the electron, b) emission of the fluorescent X-ray [29].

It should be noted that the occurrence rate of the photoelectric effect interaction is influenced by the effective atomic number of the material and the materials with higher effective atomic number tend to have higher probability of the photoelectric effect occurring.

The phenomenon was first described be Einstein [30], and has been extensively researched and expanded since then. In particular, Born provided an approximation of the photoelectric cross-section from s-states [31]:

$$_a\sigma_{ns}^{BA} = \frac{4\sqrt{2}Z^5\alpha^4}{n^3}\left(\frac{mc^2}{E}\right)^{7/2}\varphi_0 \quad (11)$$

Here m is the electron rest mass, c is the speed of light, n is the principal quantum number of the bound s-state from which the electron is ejected, α is the fine structure, and φ_0 is the cross-section for Thomson scattering. We can find the fine structure as [32]:

$$\alpha = \frac{e^2}{\hbar c} \quad (12)$$

Here *e* refers to the electron charge, ħ is the Dirac's constant.

The Thomson cross-section can be defined as [32]:

$$\frac{8}{3}\pi\left(\frac{e^2}{mc^2}\right)^2 = {}_e\sigma_{thompson} = \varphi_0 \quad (13)$$

From this equation, the cross-section per electron can be derived as:

$${}_e\sigma_{np} = \frac{1}{3} * \frac{n^2-1}{n^5}\left(\frac{\varepsilon_K}{E}\right) {}_e\sigma_{1s} \quad (14)$$

Where ε_K is the magnitude of the theoretical K-shell binding energy and is given as [28]:

$$\varepsilon_K = \frac{Z^2 m e^4}{2\hbar^2} \quad (15)$$

However, this model is not valid when $h\nu \geq \varepsilon_K$. Also, several other limitations made Born approximation unreliable on the lower energy range. In order to refine the model, several additions have been introduced over the course of the 20th century to allow for more precise parametrization.

In non-relativistic limit, the Born's approximation with plane waves gives the following formula for the cross-section for emission for the s and p states [33]:

$$\sigma_{1s}^{BA} = 4\sqrt{2}Z^5\alpha^4 * \left(\frac{mc^2}{E}\right)^{7/2}\varphi_0 \quad (16)$$

$$\sigma_{1s}^{BA} = \frac{1}{3} * \frac{n^2-1}{n^5}\left(\frac{\varepsilon_K}{E}\right) {}_e\sigma_{1s} \quad (17)$$

The following corrections have been introduced by Jackson and Hawkes [28] based on the paper by Stobbe [34].

1) The plane waves are replaced by the hydrogen like function, introducing a new multiplicative term:

$$S(E,Z) = 2\pi * \left(\frac{\varepsilon_K}{E}\right)^{0.5} * f(n_1) \quad (18)$$

Where

$$n_1 = \left(\frac{\varepsilon_K}{E - \varepsilon_K}\right)^{1/2} \quad (19)$$

$$f(n_1) = \frac{\exp(-4 * n_1 * cot^{-1} n_1)}{1 - \exp(-2\pi * n_1)} \quad (20)$$

2) The relativistic effects established by Sauter in 1931 [35] are incorporated through the factor:

$$1 + F(\beta) = 1 + 0.143\beta^2 + 1.667\beta^8 \quad (21)$$

Where:

$$\beta = \frac{\vartheta}{c} = \sqrt{\frac{2E}{mc^2}} \quad (22)$$

3) Screening by the atomic electrons, which is tabulated as a function of the effective atomic numbers by Jackson and Hawkes [28]: N(Z) (see the Appendix A). As the values for the factor N(Z) are only given for the pure materials, the 1D interpolation is utilized in order to calculate the values for the non-integer compound and mixture effective atomic numbers. The particular method used in this study is shape-preserving piecewise cubic interpolation [36] The interpolated value at a query point is based on a shape-preserving piecewise cubic interpolation of the values at neighboring grid points.

In this case the final expression for the photoelectric cross-section as presented in this work becomes:

$$_e\sigma^{photoelectric} = 4\sqrt{2} * Z^5 * \alpha^4 * \left(\frac{mc}{E}\right)^2 * \frac{8}{3}\pi\left(\frac{e^2}{mc^2}\right)^2 * 2\pi * \left(\frac{\varepsilon_K}{E}\right)^{0.5} * \frac{\exp(-4*n_1*cot^{-1}n_1)}{1-\exp(-2\pi*n_1)} * N(Z) * (1+F(\beta))^2 \quad (23)$$

However, it should be noted that since the electron density term presented in the equation (3) contains the multiplication by the electron density, the overall term *F(E,Z)* that describes the photoelectric effect component in the x-ray interaction with the matter is calculated as:

$$F(E,Z) = 4\sqrt{2} * Z^4 * \alpha^4 * \left(\frac{mc}{E}\right)^2 * \frac{8}{3}\pi\left(\frac{e^2}{mc^2}\right)^2 * 2\pi * \left(\frac{\varepsilon_K}{E}\right)^{0.5} * \frac{\exp(-4*n_1*cot^{-1}n_1)}{1-\exp(-2\pi*n_1)} * N(Z) * (1+F(\beta))^2 \quad (24)$$

Parametrization for the x-ray scattering effects

The x-ray scattering that occurs in the range of diagnostic energies (20-150 keV) can be subdivided into coherent and incoherent scattering.

Coherent scattering (also known as elastic or Rayleigh scattering) occurs when the energy of the incoming photon is relatively small in comparison to the ionization energy of the atom and is more prevalent on the lower energy spectrum. As the photon energy is below the binding energy of the electron, the electron is not ejected from is orbit and no energy transfer occur, thus the photon continues traveling with the same energy, albeit at a change angle. As no energy occurs, there is no ionization happening with this type of interaction either. The summarized effect of the coherent scattering can be demonstrated by the following diagram:

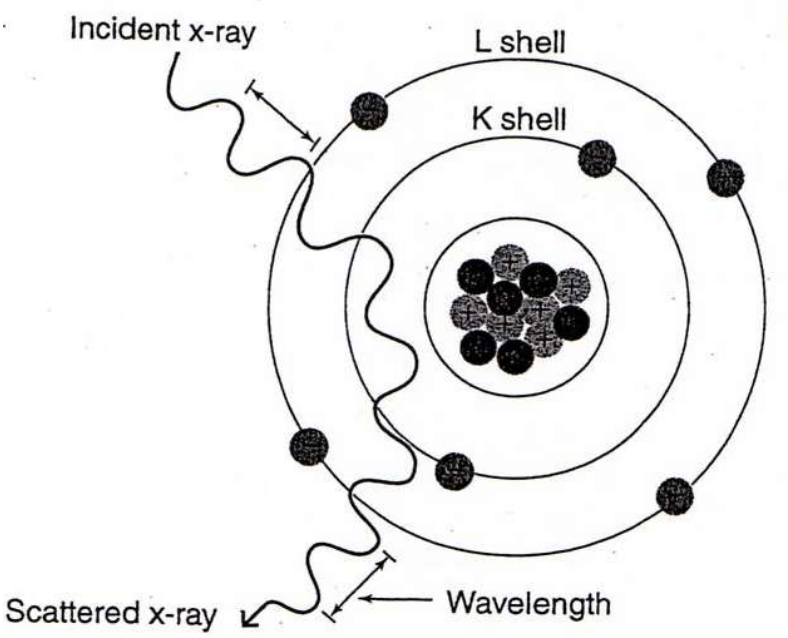

Figure 5 - Coherent scattering. Wavelength of the photon, and, consequently, its energy, does not change [37]

The total cross-section for the coherent scattering is given by [28]:

$$_a\sigma^{coh}(Z,E) = \int d\sigma^{Th}(\theta)F^2(x,Z) \quad (25)$$

Here θ refers to the scattering angle, F is the atomic form factor, tabulated by Hubbel et. al. [32] (see Appendix B), and x is momentum transfer variable that can be found as:

$$x = \frac{E}{hc}\sin(\frac{\theta}{2}) \quad (26)$$

We can rewrite the equations 19 and 20 so that:

$$\sigma^{coh} = \frac{3}{8}\sigma_T \int_{-1}^{+1}(1+cos^2\theta)[F(x,Z)]^2 dcos\theta \quad (27)$$

$$x = \frac{E}{hc} * \sqrt{\frac{1-cos}{2}} \quad (28)$$

And integrate over the range from -1 to 1.

Unfortunately, this model is not straightly applicable to our case due to comparatively high inaccuracies for the lighter elements found in the human tissues. This matter, however, can be solved by using the etalon cross-section. According to Thomas-Fermi model [38] we can relate the coherent cross-section of any given element to the cross-section of to the cross-section of the etalon element Z', in this case chosen to be oxygen (Z(O) = 8). Adjustment of the etalon element should be made for the range of the suspected materials when calculating the effective atomic number. The relation between the two cross-sections can be expressed as:

$$ {}_a\sigma^{coh}(Z,E) = (\frac{Z}{Z'})^2 * {}_a\sigma^{coh}(Z',E') \quad (29) $$

Where:

$$ E' = (\frac{Z}{Z'})^{1/3} * E \quad (30) $$

$$ {}_a\sigma^{coh}(Z',E') = \frac{3}{8}\sigma_T \int_{-1}^{+1}(1+cos^2\theta)[F\left(\frac{E'}{hc} * \sqrt{\frac{1-cos\theta}{2}}, Z'\right)]^2 dcos\theta \quad (31) $$

The incoherent scattering (also known as inelastic, or Compton scattering) is a process where the incoming photon hits the outer-shell electron with enough force to dislodge it from its orbit, thus creating a vacancy. However, the photon itself is not completely absorbed, but rather continues to travel, albeit with a change of direction (expressed by the scattering angle θ) and a loss of energy. The vacancy in the outer shell causes the atom to ionize, thus Compton scattering is considered an ionizing radiation. The summary of the Compton Effect interaction can be presented on the following diagram:

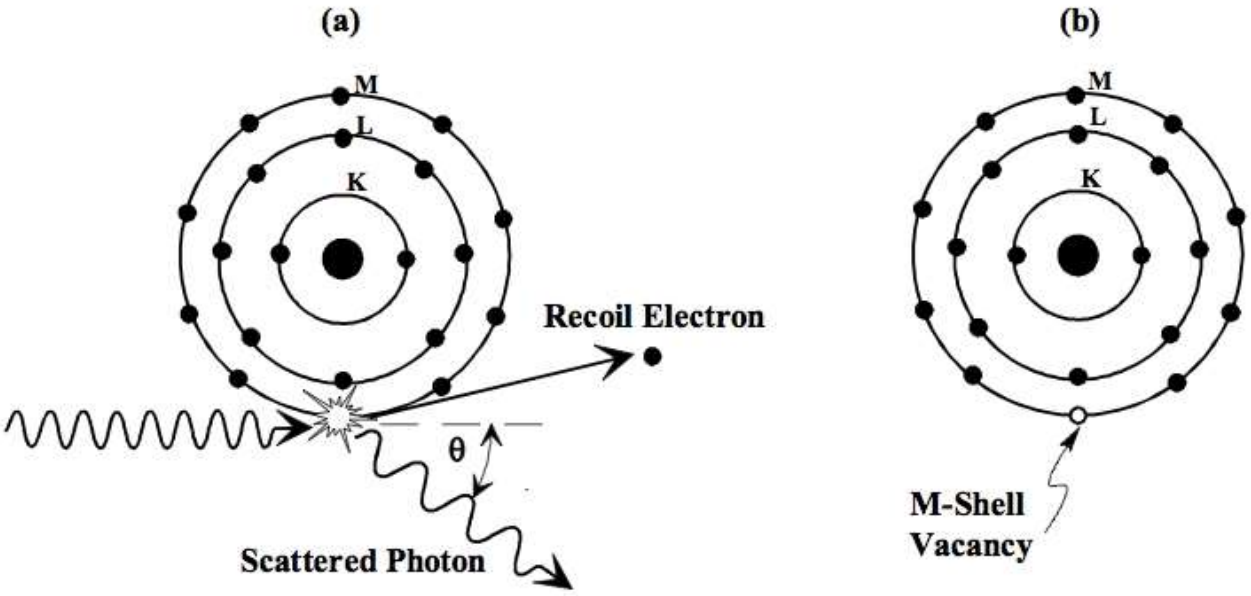

Figure 6 - Compton effect, where the photon hitting the electron and causing its ejection leads to the ionized atom. Image courtesy of [39]

The incoherent scattering cross-section can be presented as:

$$_a\sigma^{inco}\ (Z,E) = \int d\sigma^{KN}(\theta)S(x,Z) \quad (32)$$

Where $\sigma^{KN}(\theta)$ refers to the Klein-Nishina cross-section [40] and S(x,Z) is the incoherent scattering function tabulated in [32].

We can calculate the Klein-Nishina cross-section by the following formula:

$$_e\sigma^{KN} = 2\pi * r_e^2 * (\frac{1+k}{k^2} * \left[\frac{2(1+k)}{1+2k} - \frac{\ln(1+2k)}{k}\right] + \frac{\ln(1+2k)}{2k} - \frac{1+3k}{(1+2k)^2}) \quad (33)$$

The common approximation of the incoherent cross-section $_a\sigma^{incoh}(Z,E) \propto Z\sigma^{KN}(E)$, however, according to Jackson et al, is not satisfactory at the E < 100 keV. Instead, we may utilize the relation:

$$Z\sigma^{KN}(E) - \ _a\sigma^{incoh}(Z,E) \approx f(Z)Z^{-1}\ _a\sigma^{coh}(Z,E) \quad (34)$$

In which, for E > 30 keV, $f(Z) = Z^b$, where b = 0.5 and is determined empirically by being the best choice over the range of effective atomic number values encountered in

the tissue. In case of iodine contrast agent with significantly higher effective atomic number, further adjustments are required.

Combination of the equations 29 and 33 gives us the following relation:

$$ {}_a\sigma^{coh}(Z,E) + {}_a\sigma^{incoh}(Z,E) = \mathrm{Z}\sigma^{KN}(E) + (1 - Z^{b-1})(Z/Z')^2 \, {}_a\sigma^{coh}(Z',E') \quad (35) $$

Which we can further divide by Z (equation 3) to get the scattering term G(Z,E):

$$ G(Z,E) = {}_e\sigma^{KN} + \frac{1}{Z}(1 - Z^{b-1}) * (\frac{Z}{Z'})^2 * \sigma^{coh}(Z',E') \quad (36) $$

And with this we can solve for the effective atomic number Z by acquiring to sets of data for different energies and different corresponding attenuation coefficient and solving the following equation:

$$ Z^4 - \frac{\mu(E_2)G(E_1,Z) - \mu(E_1)G(E_2,Z)}{\mu(E_1)F(E_2,Z) - \mu(E_2)F(E_1,Z)} = 0 \quad (37) $$

By minimizing Z.

In this particular work, the medium-scaled algorithm based on the trust-region dogleg method was utilized [36]. It is based on the Powell dogleg method and is implemented in the Matlab Optimization Toolbox as a nonlinear system iterative solver. The method includes the choice of trust region that approximates the objective function in a ball. The size of trust region is chosen in accordance with the range of the function. The Dogleg method is the combination of the steepest descent and Newton optimization methods. The initial guess assigned at the beginning of the iterations is the same as the etalon element (oxygen, Z = 8). Further details on the algorithm performance can be found in [41].

Effective atomic number for the whole spectrum

In order to find the effective atomic number across the whole range of the energy spectrum, alternative iterative method is utilized. The initial guess is made for the effective atomic number Z based on the empirical evidence. This initial guess is then used to construct the system of linear equations:

$$\mu_i = \rho_e[Z^4 * F(Z, E_i) + G(Z, E_i)] \quad (38)$$

With i = 1… n corresponding to the number of measurement in the measurement series (n = 6 for the contrast phantom and n = 9 for the iodine contrast agent phantom). The assumption about the electron density is made for it to be close to water electron density of ρ_e = 3.34*10^{-29} el/m^3. The system is solved as a system of linear equations and the approximate solution for the first iterations is found. The approximate solution is compared to the initial guess and should it surpass a certain error margin, next iteration is in order. The approximate solution for Z is then utilized for the next iteration as an initial guess and the process is repeated until the difference in the solutions between iterations becomes negligible. This allows us to establish the overall effective atomic number across the whole spectrum.

The code for the physical model of linear attenuation coefficient constituents can be found in Appendix C.

Objects of study

The following study concentrated on two different types of phantoms.

Contrast phantom

Contrast phantom presents an acrylic (water-equivalent) tube (2.5 cm in diameter) with 5 hollow tubes (5 mm in diameter) filled with the various materials. The fillings include calcium chloride powder, air, water, oil (pure olive cooking oil), and 5% iodine disinfection solution. The schematic and physical representation of the contrast phantom and the can be found below:

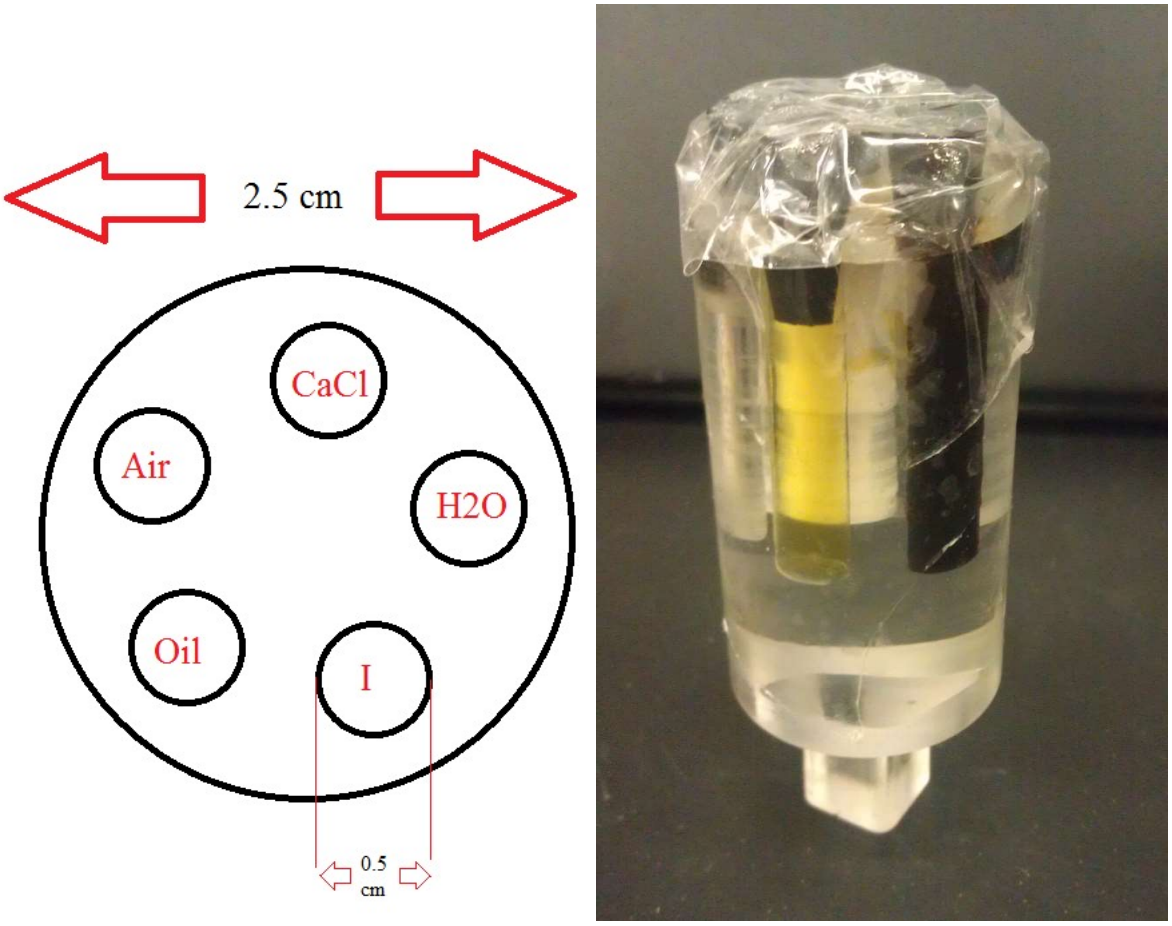

Figure 7 - Contrast phantom

The second phantom utilizes the same geometrical set-up. The hollow tubes are filled with the Omnipaque contrast phantom solution mixed with water. The concentrations of iodine evaluated in the study are 35 % (pure Omnipaque solution), 28 % (80 % Omnipaque and 20 % water), 21 % (60 % Omnipaque and 40 % water), 14 % (40 % Omnipaque and 60 % water), 7% (20 % Omnipaque and 80 % water).

The CT system set-up, geometrical calibration and scanning protocol

The CT system set-up

The CT system consists of the following parts:

1) X-ray source
2) X-ray source Aluminum filter
3) Rotating object stage
4) X-ray color detector – eV3500
5) X-ray detector Lead filtration
6) X-ray detector Aluminum filtration (inbuilt)

The schematics of the CT system are presented on the following figure:

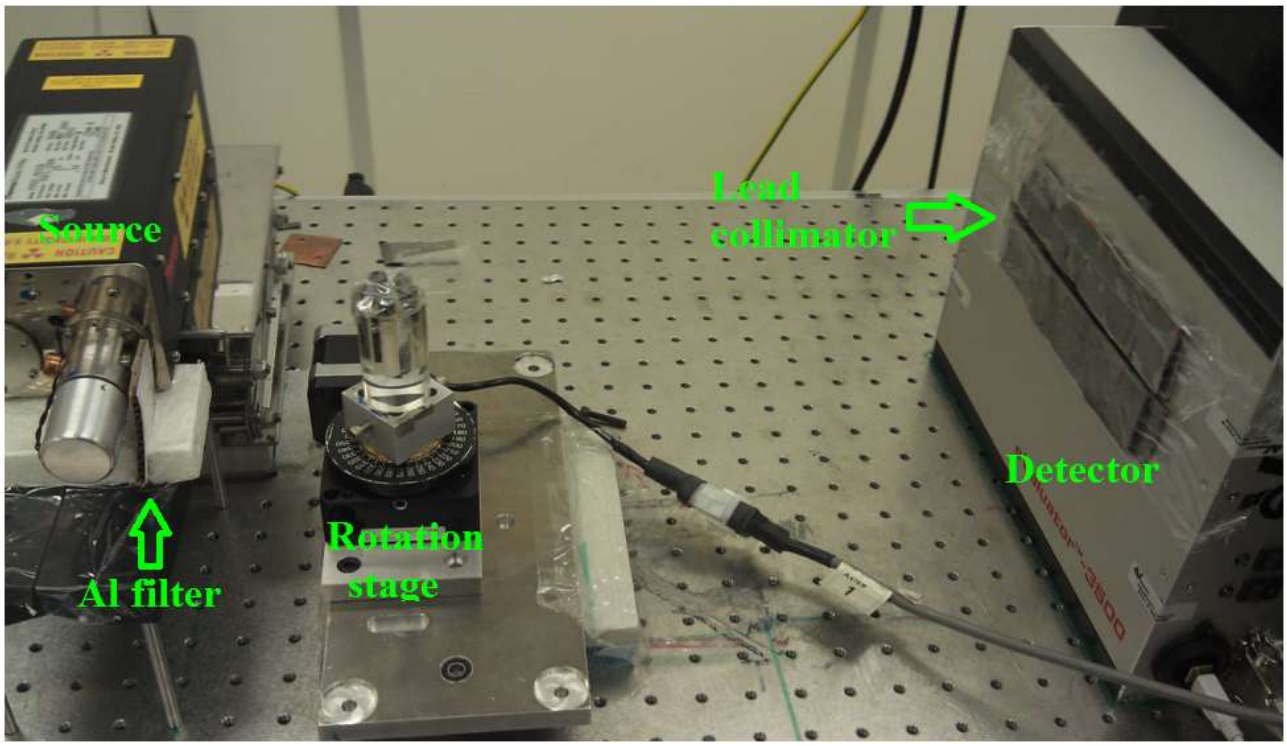

Figure 8 - CT system set-up

Each system component can be described as:

1) X-ray source: KEVEX, polychromatic cone-beam x-ray source
2) X-ray source aluminum filter: presented by the 2 mm thick aluminum plate that obscures the x-ray source window and shifts the x-ray spectrum curve towards higher energy
3) Rotating object stage: fixed rotation stage that allows for 360 degrees rotation of the object at the chosen incremental step. The rotation stage movement is controlled by the in-house LabView software developed in the X-ray systems lab. The motor controller is Velmex VXM-3.
4) X-ray color detector eValuator 3500: a fully integrated Photon Counting energy discriminating CZT (Cadmium Zinc Telluride) linear detector. This includes an onboard microcontroller and FPGA allowing true "real time" operation. Five energy bins are available, with the minimum width of the bin being 5 keV and threshold uncertainty level being ± 2.5 keV. The detector consists of 256 detector pixels, each 0.5 mm wide and 2 mm in height (as denoted by the red line). The detector operates with 160 ns peaking time and 250 μs acquisition time. The detector is covered with 1 mm Al plate, creating an additional filtration for the incoming x-ray.
5) X-ray detector lead filtration is introduced in order to reduce the effects of scattering that are generated due to the cone-beam nature of the x-ray beam exiting the x-ray source. As the detector utilized in the study is a linear detector, fan-beam like geometry at the detector site is achieved by placing 6 mm thick lead filter at the detector surface.

The CT system scanning protocol

The CT system geometry is set up so that the magnification factor for the object real size to its appearance on the detector site would be 4X. Magnification is calculated

as the ratio between the source to detector distance (SDD) and source to isocenter distance (SID):

$$M = \frac{SDD}{SID} \quad (39)$$

$$Pixel\ size\ at\ the\ isocenter\ = Detector\ pixel\ size/M \quad (40)$$

In our particular scenario the SID = 116.7 mm, SDD = 467 mm, magnification factor is 4X, pixel size at the isocenter of the scanned object = 125 μm (0.5 mm/4).

An important part of the CT system set-up is establishment of the rotational axis offset. In the ideal fan-beam geometry, the shortest distance between the source and the detector is the distance between the source (approximated as a fan vertex) and the exact middle of the detector, which in the case of 256-element long linear detector is the point between element 128 and 129, and is denoted as the detector FOV physical center. In this case we denote the ray connecting the vertex and the detector center as the central ray. We also have to introduce the concept of the piercing point – the intersecting point of the detector with the line connecting the source point and the rotation axis. In the ideal case scenario the piercing point, the physical center of the detector, and the rotation axis all correspond to the same coordinates, and thus no adjustments have to be made for the acquired sinogram. However, that is not always the case in real life, and some offset is always present between the piercing point and the physical center of the detector. For the cone-beam CT, a combined experimental-analytical method developed by F. Noo et. al has long been utilized and is well-described in the literature [42].

However, for the fan-beam CT, no such method exists. The only methods for the fan-beam calibration available in the literature involve the utilization of the specific pencil-beam collimator positioned at the source site, and subsequent detector illumination so that only a single detector pixel is illuminated at a time. Unfortunately, such an approach is not practical at a time, as it would require for the collimator hole

to be so small that even after the magnification the pencil ray width would not exceed that of one pixel.

Instead, the author of this thesis has developed as alternative approach that allows for the offset calibration. Instead, a phantom consisting of two thin metal needles is utilized. The first needle is positioned exactly at the center of rotation so that the initial location of the rotational axis can be estimated by a short series of projections taken at 0, 180 and 270 degrees. This needle will be presented as a straight line on the sinogram as its position changes very little during the rotation of the phantom. The second needle is positioned at the certain distance from center, so that the sinogram formed by this needle will resemble the sine curve as the angular position of the needle in comparison to the starting point changes. The first needle is 0.6 mm in diameter, made of stainless steel, and is hollow in the middle. The second needle is 0.8 mm in diameter, made of stainless steel, and is hollow in the middle. Both needles are deposited inside the hollow acrylic tube 2 cm in diameter and are prevented from the movement during the object stage rotation by the Styrofoam deposited inside the tube. The phantom utilized for the geometrical calibration is presented on the figure below:

Figure 9 - Geometry calibration needle phantom

The sinogram formed by the needle phantom scan is presented on the next figure:

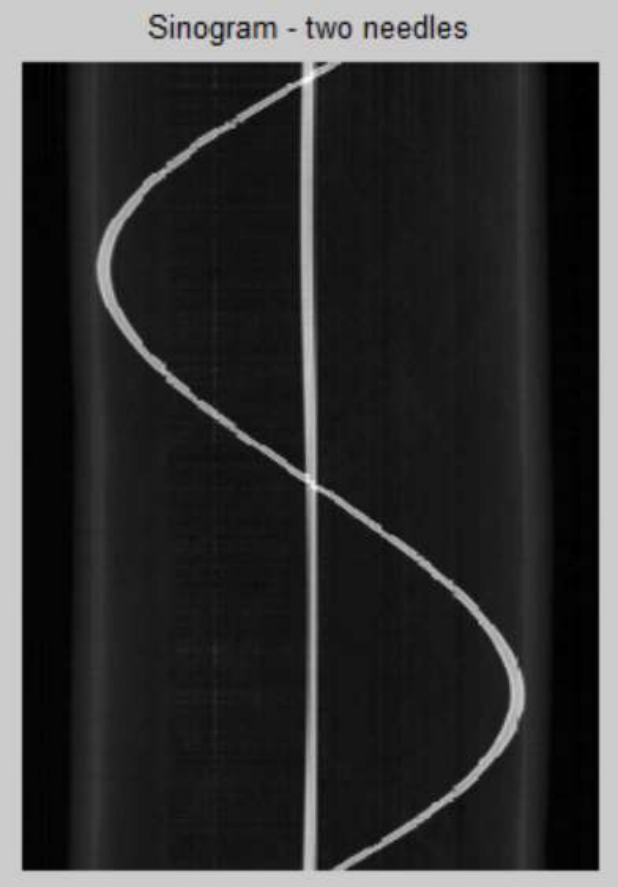

Figure 10 - Sinogram of the 4X needle phantom scan

As can observed on the figure above, the needle positioned at the center experience very small range of movement which can be attributed to the needle vibration between different angle scans, as well as the needle inherent inhomogeneity in structure, as it is not ideally cylindrical. The second needle presents a noticeable sinusoidal arc typical for this type of geometrical positioning of the object in comparison to the rotational axis.

The sinogram is then used for the reconstruction process described in the previous chapter. The resulting image slice is presented in figure below:

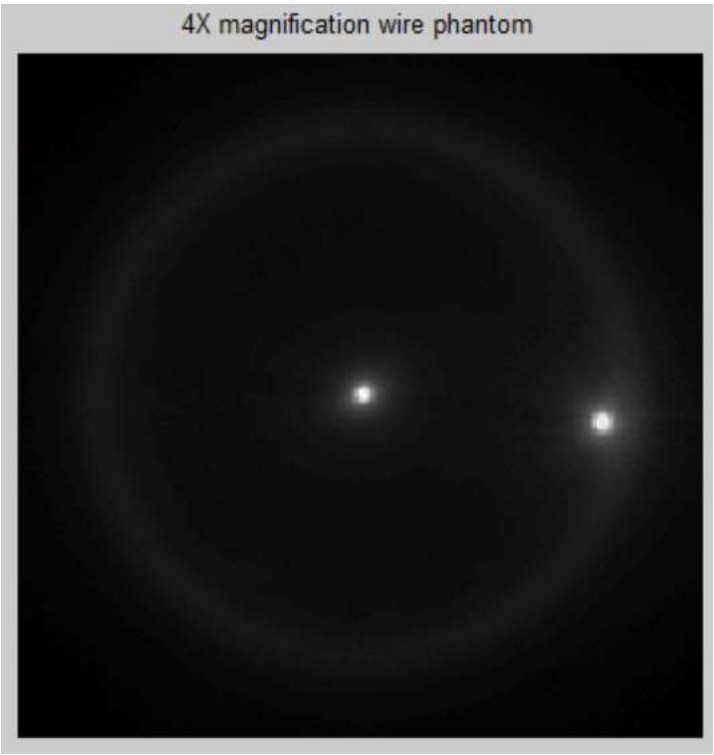

Figure 11 - Reconstructed needle phantom slice

As can be seen, the needles appear to be of regular shape, with the first needle being positioned at the center of the phantom and the second needle being positioned near the acrylic wall. In addition, the acrylic wall itself is easily observed on the figure above, indicating the difference in the attenuation coefficient of the acryl (equivalent to water) and surrounding air (and air-equivalent Styrofoam).

The close look at the reconstructed needles reveals that the number of pixels denoted by the higher attenuation coefficient corresponds to the size of the corresponding needle recalculated due to the magnification factor, and their shape appears to be regular, indicating correct offset detection.

A) 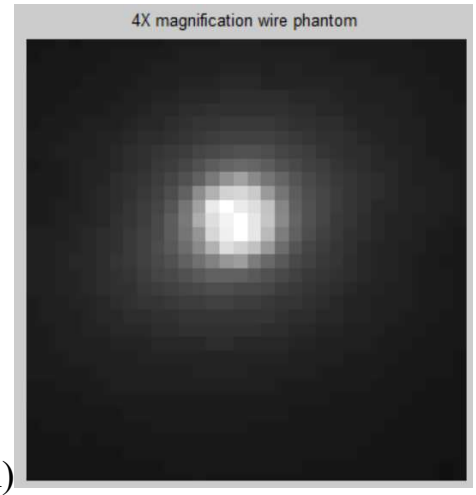

B) 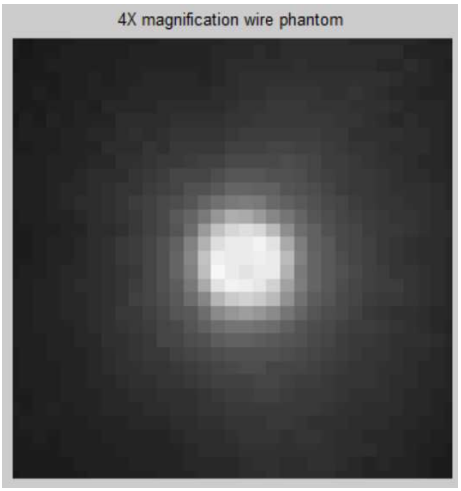

Figure 12 - A) Close look at the central needle, expected to span across 4.8 pixels, B) Closer look at the wall needle, expected to span across 6.4 pixels.

The detector response calibration

The detector response calibration plays an important in understanding how the projection reading is acquired and whether or not the detector response is stable throughout the time and from pixel to pixel. Two types of stability have to be considered before the correction factor for the detector response variation can be implemented. Temporal stability shows the variation in the response of a single pixel over the typical length of the scan (time necessary to take 360 projections). Spatial stability shows the variation in response from pixel to pixel within a single projection, with signal for every pixel being acquired simultaneously. A short study presented above shows the scope of the detector response variability and presents the correction method utilized in this study that was developed by the author of this thesis.

Temporal stability evaluation

The CT scan is performed in accordance with the following parameters:

Acquisition time: 1 second

Peak voltage: 65 kVp

Current: 0.015 mA

SDD: 467

Energy bins: 20-30 keV (1 bin), 30-40 keV (2 bin), 40-50 keV (3 bin)

Only the data acquired at the first three energy bins is routinely used in reconstruction due to the intended energy range constraints for bin 4 and 5.

The blank projections are acquired for the duration of 50 minutes, which is the usual time for one CT scan. The 72 projections are taken at every 40 seconds mark – the average time to acquire 5 projections In 360 projection scan.

First, the values recorded by the detector for every bin are plotted out for every 12^{th} blank projection (every 8.33 minute interval). The colors utilized for the line profiles are blue, red, green, yellow, cyan, magenta and black, line profiles overlapping below:

A)

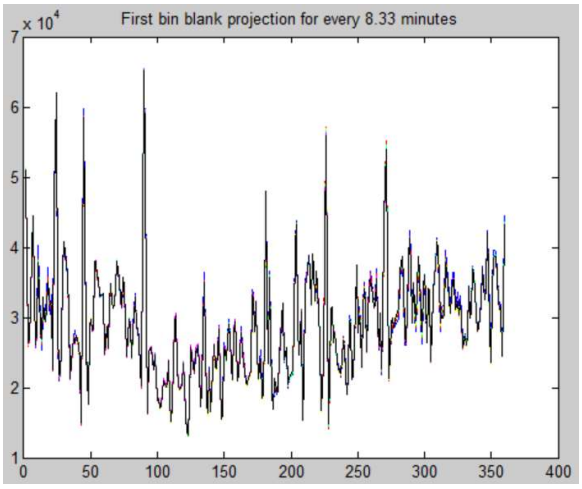

B)

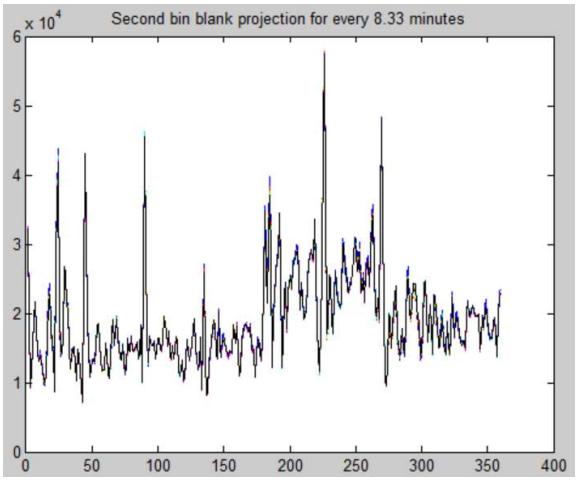

C)

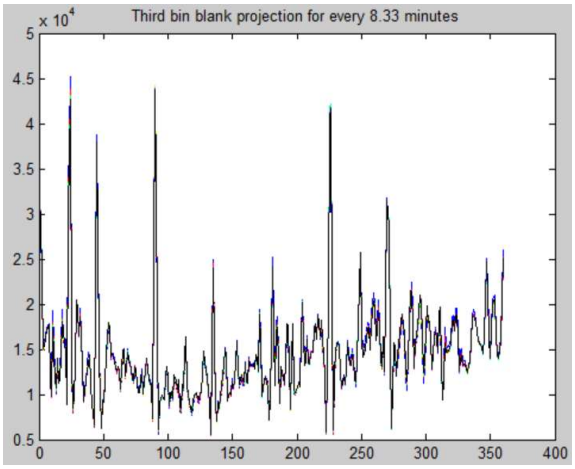

Figure 13 - Blank projection with overlapping readings from selected time points. A) 20-30 keV bin; B) 30-40 keV bin; C) 40-50 keV bin

The figure above demonstrates low variation in a single pixel response over time. In order to confirm this observation, we investigate the comparison between a single selected projection (blue) and the mean value for all projections taken during the 50 minutes period (red):

A)

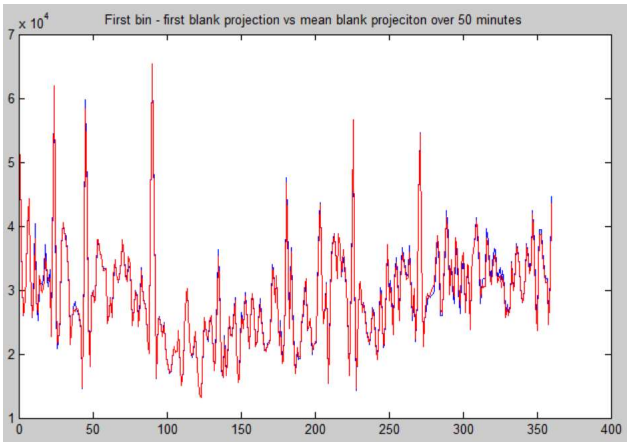

B)

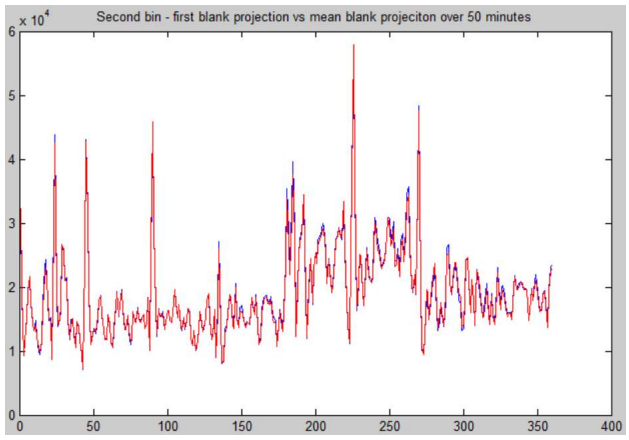

C)

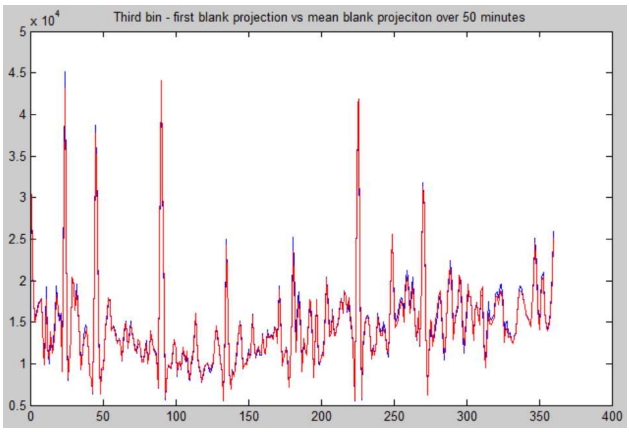

Figure 14 - Comparison between a single observation and mean values for A) 20-30 keV bin; B) 30-40 keV bin; C) 40-50 keV bin

Next, we can compare the standard deviation for the projections taken over 50 minutes for each energy bin:

A)

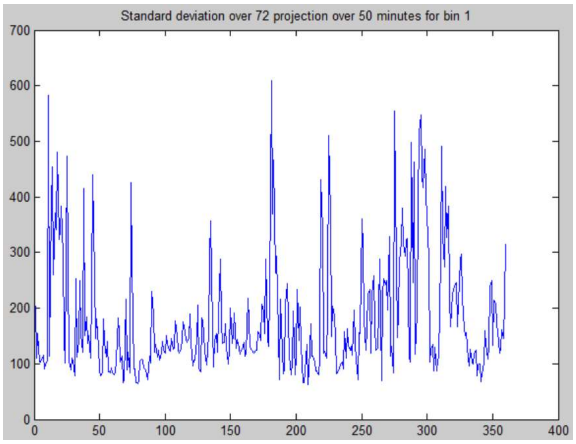

B)

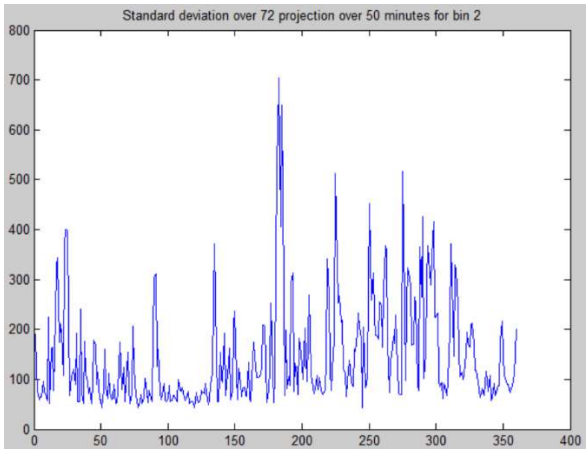

C)

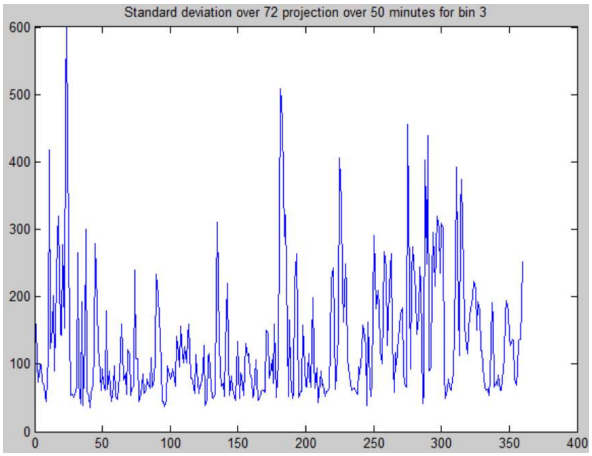

Figure 15 - Standard deviation of individual pixel response over 50 minutes time period for A) 20-30 keV bin; B) 30-40 keV bin; C) 40-50 keV bin

In addition, we can compare the magnitude of the standard deviation to the magnitude of the overall blank projection by utilizing the following formula:

$$\% \text{ time variation} = \frac{std}{blank\ projection} * 100 \quad (41)$$

The calculated values are presented in the following figure:

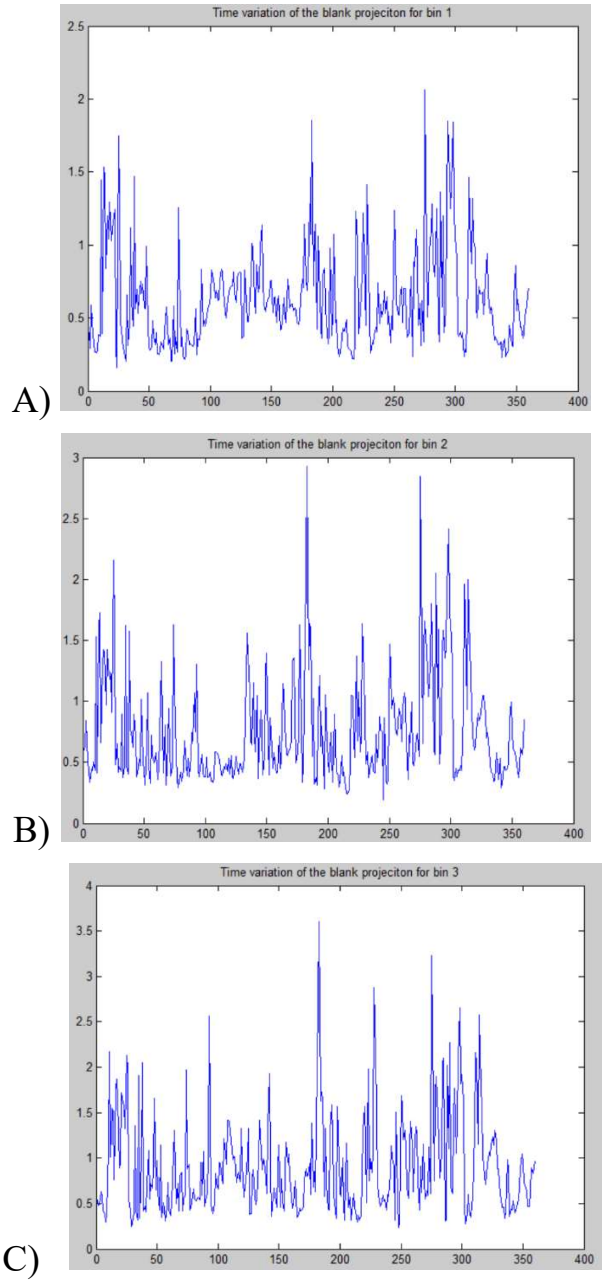

Figure 16 - Time variability in percentage for A) 20-30 keV bin; B) 30-40 keV bin; C) 40-50 keV bin

As can be observed from the presented plots, for bin 1 (20-30 keV) the average time variation is within 0.6307 %, for bin 2 (30-40 keV) the average time variation is within 0.7613 %, for bin 3 the average time variation is within 0.9126 %. Overall, the time variation in the blank projection over the time period of 50 minutes is negligible and shouldn't affect the applicability of the blank projection taken over short period of time (1 minute) to the whole CT scan projection data.

Spatial stability of the detector

The eV-3500 detector demonstrates high spatial variability in the measurements from pixel to pixel for the fan-beam of the same voltage and current taken over the same period. The system response in terms of spatial stability varies from bin to bin. On the graph below, we can see the variation in response for bin 1 and the polynomial approximation of the 4th order for the average response:

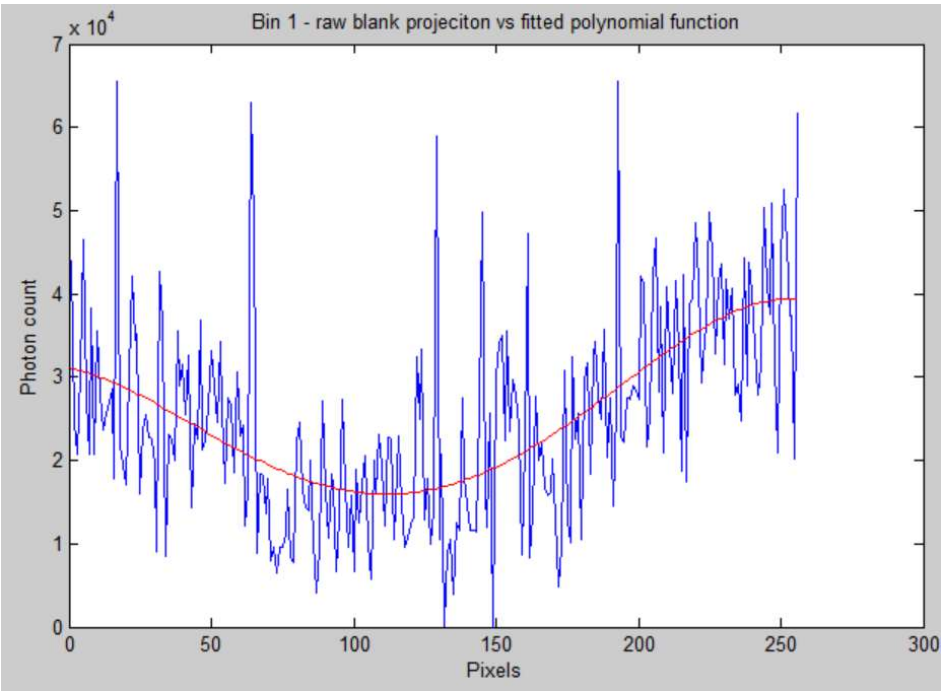

Figure 17 - Bin 1 spatial variability and response curve

As can be seen from the figure 16, the detector response seems to follow a paraboloid curve. For the bin 2, additional challenge is present in forming the detector response function, as the inherent defect of the gain calibration between four plates that form the detector surface, with each plate covering 64 pixels, make the response for the plate 3 of the bin 2 significantly elevated in comparison to its neighbors:

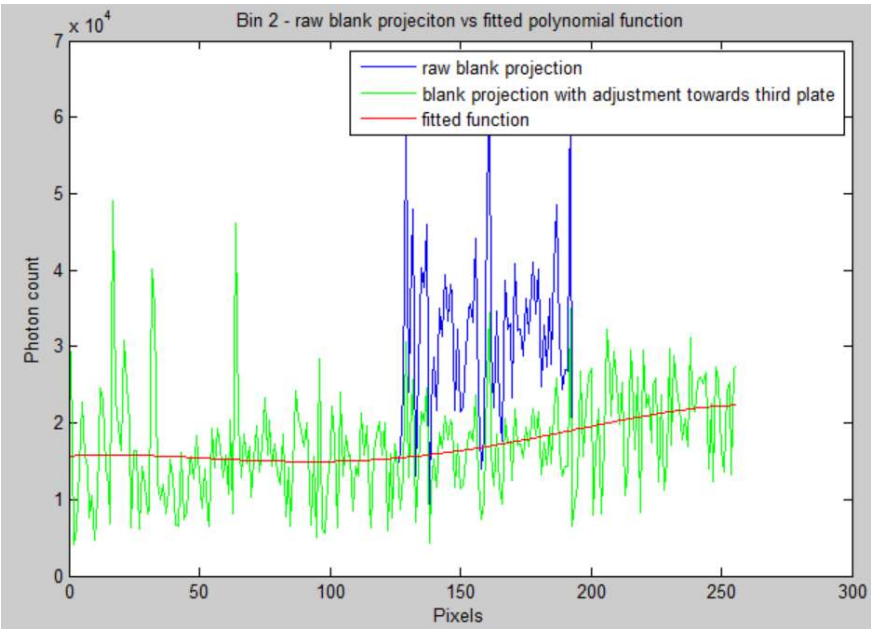

Figure 18 - Bin 2 spatial variability and response curve

As can be seen, special adjustments have to be made in order to fit the response from the pixels 128-192 along with the rest of the pixel response. The paraboloid curve is less pronounced in the bin 2.

Similarly to bin 1, in bin 3 all plates generate continuous response:

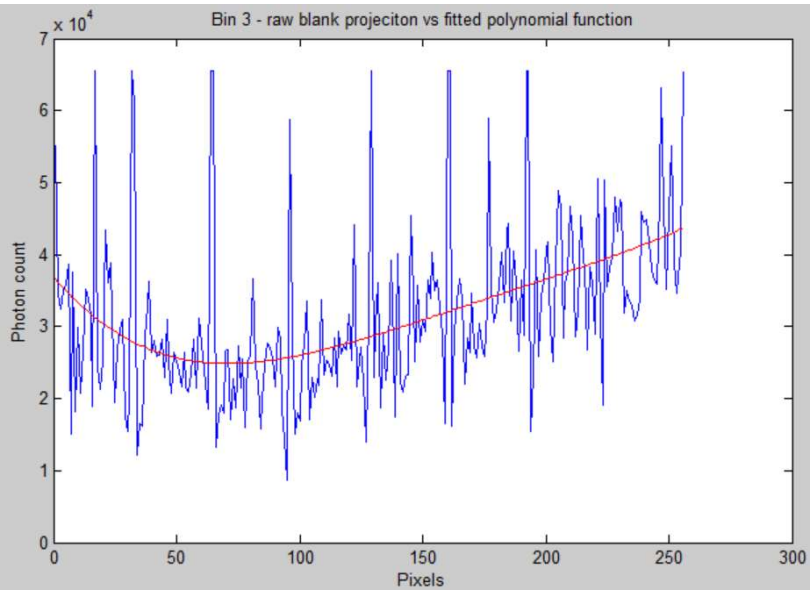

Figure 19 - Bin 3 spatial variability and response curve

The paraboloid approximation of the average detector response in skewered to the left. It should be noted that the same response pattern repeats for bin 1, 2 and 3 regardless of the chosen energy setting and energy window width selected, so the patters follows the inherent electronic layout of the detector. Average bin count pattern with 0.5 Al filtration stays constant across the energies and scanning protocol variation:

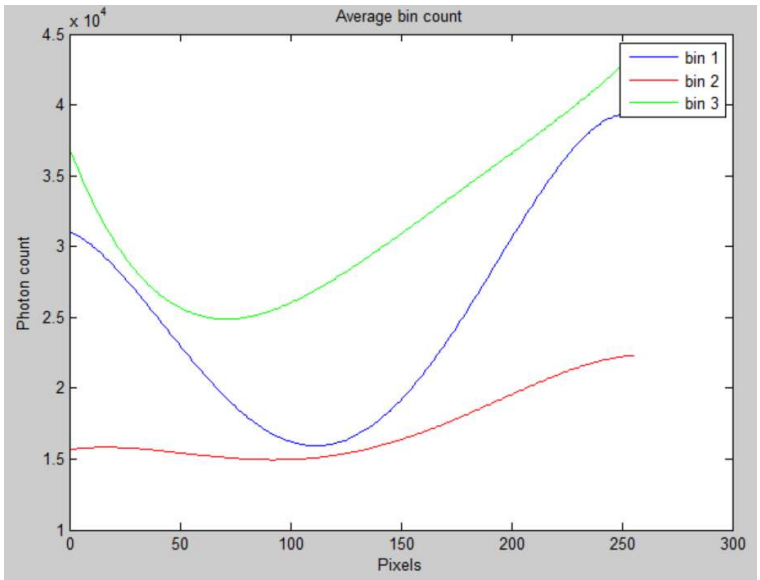

Figure 20 - Spatial variability curves across the three bins utilized for the signal acquisition

The corresponding correction factors are introduced to initial signal processing in order to generate a smooth sinogram. The calculation of the correction factors is performed in accordance with the following protocol:

1) Initial blank projection acquisition
2) Calculation of the polynomial function for the blank projection that would provide for the overall pixel response curve
3) Calculating the expected individual pixel's response in accordance with the fitted polynomial curve. The value for each expected individual pixel's response is saved.
4) Calculating the offset of the real vs expected pixel response by comparing the acquired count and the expected count on the pixel-to-pixel basis for the blank projection. The offset value is saved as the correction factor.
5) Applying the correction factor calculated in previous set to the photon count reading obtained for the object scan.

As the result of the protocol described above, a smoother projection photon count can be obtained, as demonstrated on the following figure:

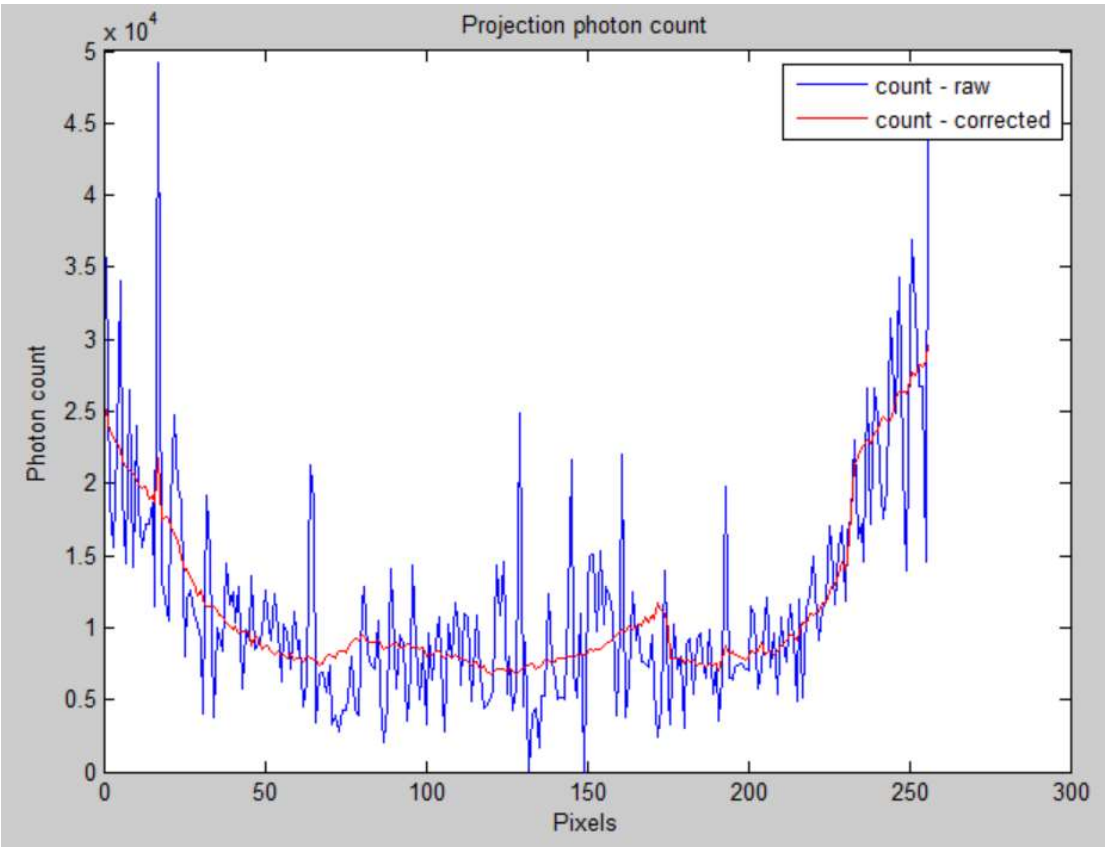

Figure 21 - Smoothing the photon count

With the smoothed pre-processed data the sinogram obtained presents more consistent data and contains less artifacts. However, the resulting sinogram is still suffering from the spatial instability that will result in the ring-shaped artifacts after the reconstruction. Thus, as additional smoothing is required in order to get rid of the most severe artifacts. The ring-artifact suppression can be subdivided into two parts:

1) Pre-reconstruction
2) Post-reconstruction

Pre-reconstruction correction

Pre-reconstruction correction refers to the manipulation of the sinogram values. The sinogram itself contains the visible stripes and regions whose values are far beyond the norm. The abnormal stripes correspond to the individual pixel's abnormal response throughout all scanning angle and demonstrate similar behavior throughout the scan's duration. In order to identify the location of these stripes, the visual inspection is performed. The example of such stripe and its identification is presented on the figure below:

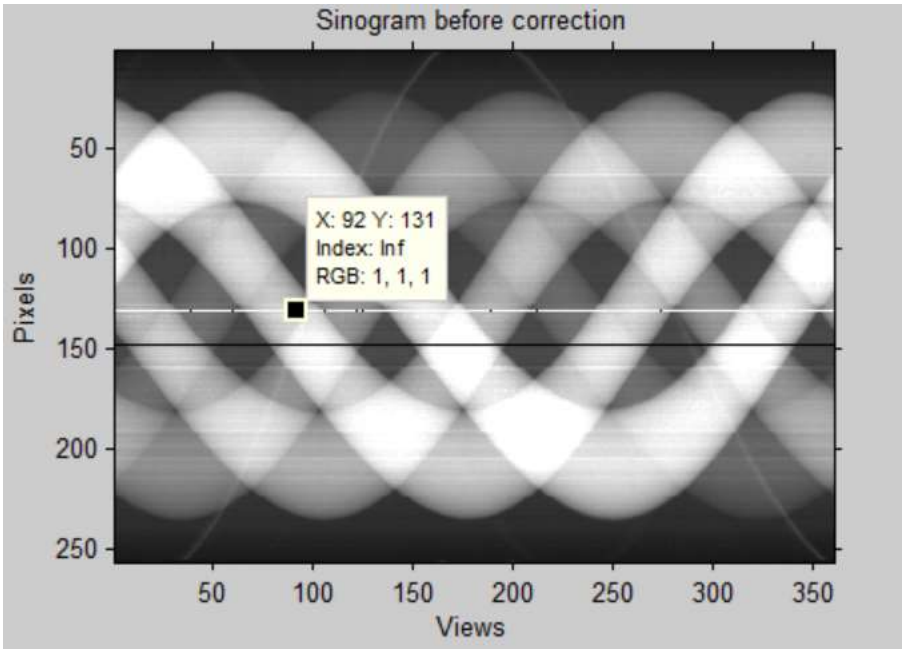

Figure 22 - Sinogram before correction with the stripe highlighting the bad pixel # 131. As the readings in this particular pixel are usually zero, the sinogram value expresses infinity.

The example above highlights only the most severe case where the pixel itself measures the zero photon count, indicating the pixel being completely broken. But even the cases where the values are slightly off the expected sinogram value can generate a

serious ring artifact. The example of such outlier reading can be demonstrated in the following figure:

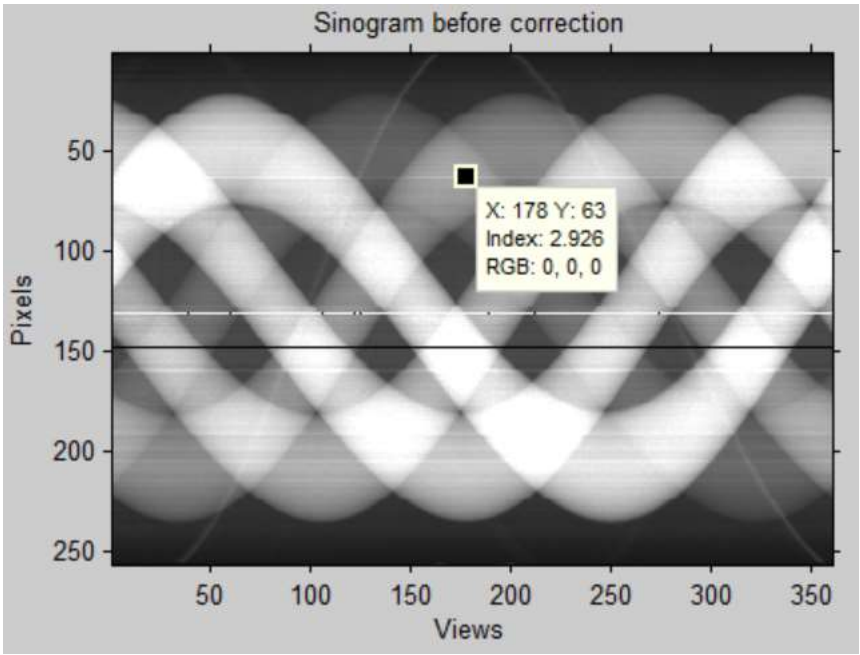

Figure 23 - Pixel # 63 expressing abnormal sinogram value.

Pixels # 64 and # 62 have the values of ≈2.5, whereas the value of pixel # 63 is 2.926, which can be considered abnormal for the smooth pattern of the sinogram. The visual inspection also reveals that all values for pixel # 63 for varying scanning angles have the same tendency to be higher than their neighbors. This observation leads us to the necessity to correct the values corresponding to pixel # 64 by calculating the approximate value based on the values of the neighboring pixels. While the linear approximation helps to smooth the sinogram values and leads to the corresponding reduction of the ring artifact severity in the reconstruction process, the sharpness of the sinogram and the subsequent reconstructed image suffers as the result. The balance has to be maintained between the ring artifact reduction and preservation of the image details. The effect is demonstrated on the figure below:

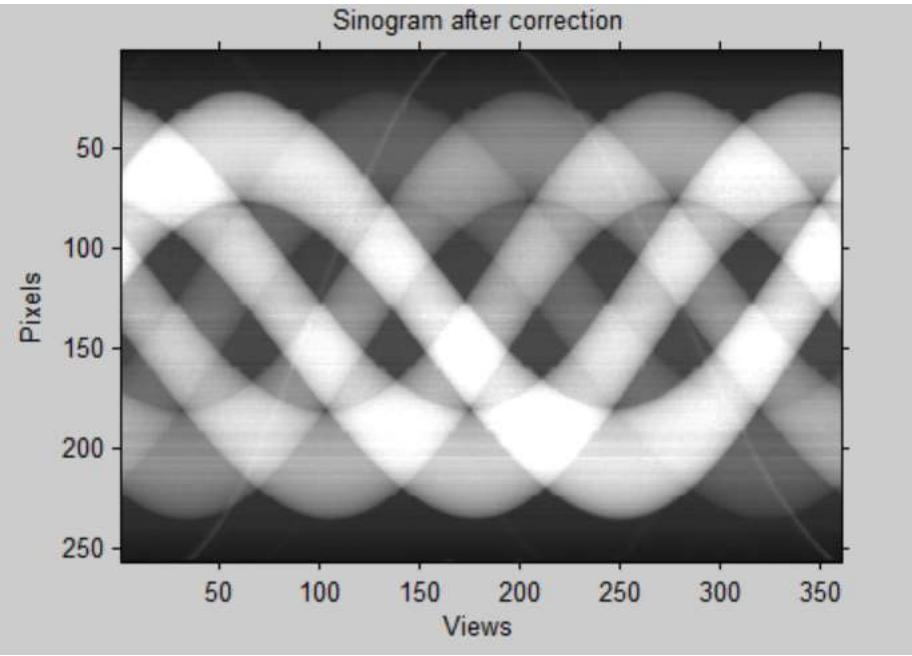

Figure 24 - Sinogram after correction

Here, it can be seen that the most severe line aberrations have been corrected via approximation of the values based on the neighboring regions. Further smoothing will cause a significant drop in the image sharpness after the reconstruction.

The reconstruction mechanism is explained below.

X-ray tomography iterative reconstruction

In the following work, the iterative reconstruction method based on the hybrid approach that combines Tikhonov regularization with Krylov subspace method has been used. In the computer tomography iterative reconstruction, the image slice can be represented by the following system of linear equations:

$$b = Ax_{true} + \varepsilon \quad (42)$$

Where $A \in R^{m \times n}$ represents the system matrix which is composed in accordance with the linear integral model [43], $x_{true} \in R^n$ is the value of the pixels in the image, ε represents the unknown perturbations in the data that can be attributed to noise, and $b \in R^m$ is the signal acquired at the detector site and processed into a sinogram. Each value of b represents the reading of one detector pixel at a certain angular position. The overall number or the detector pixels (256 pixels) multiplied by the overall number of the projections (360 projections) gives us $m = 92160$. At the same time, as we have 256x256 image matrix, the dimension of x is n = 65536. The noise in the data, termed ε, is significant in our case, which in turn makes computation of x_{true} a complex problem that requires iterative approach. We are presented with an *ill-posed* problem, as the matrix A becomes ill-conditioned and thus additional methods are required in order to apply regularization to the computation of the stable x_{true} solution. One of the most well-known forms of the regularization used these days is Tikhonov regularization [44] that amounts to:

$$\min_x \left\| \begin{bmatrix} b \\ 0 \end{bmatrix} - \begin{bmatrix} A \\ \lambda L \end{bmatrix} x \right\|_2 \quad (43)$$

Where L is the regularization operator, λ is the regularization parameter chosen so that $\sigma_n \leq \lambda \leq \sigma_1$, where σ_n is the smallest singular value of the system matrix A, and σ_1 is the biggest singular value of A. Several techniques for finding the L operator and λ parameters have been developed by utilizing generalized cross validation and singular value decomposition methods, discussed later in the chapter.

When trying to solve this problem via the traditional iterative methods such as LSQR [45], an additional problem presents itself. Up until the certain amount of iterations is run, the solution appears to come closed and closer to the truth, however, once that number of iterations has been surpassed, the algorithm starts to reconstruct the information about the noise and the solution once again diverges from the ground truth. The relative error at each iteration can be represented as:

$$error = \frac{\|x_k - x_{true}\|_2}{\|x_{true}\|_2} \quad (44)$$

And once the relative error is plotted, it is easy to establish where the divergence occurred:

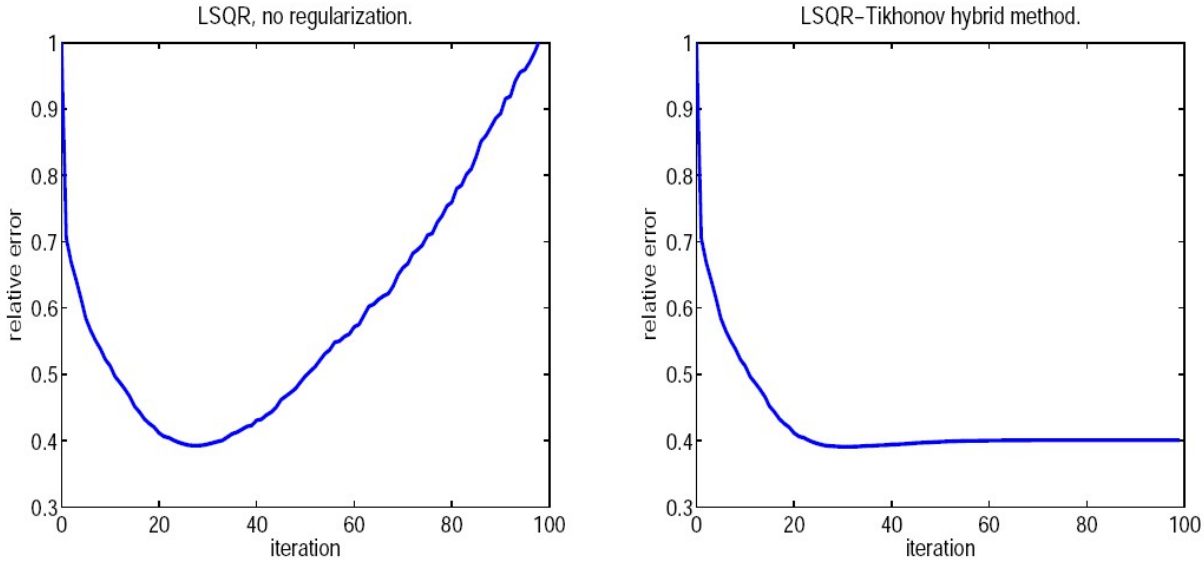

Figure 25 - Relative error's dependence on the iteration number. Left plot demonstrates the phenomenon of semi-convergence in the conventional reconstruction algorithm. Right plot demonstrates the error stabilization in the improved algorithm. Images used with permission from Dr. Chung, 2008 [46]

The hybrid method that utilizes the combined Lanczos bidiagonalization algorithm [47] with a direct regularization scheme [46] can stabilize the error and cut off the algorithm execution beyond a certain iteration. The basic idea behind the algorithm is to project the large-scale problem onto Krylov subspaces of small dimension, which can then be easily solved using regular Tikhonov regularization. The disadvantage of the approach lies in the fact that at each iteration, a new set of regularization parameters has to be recalculated. In this particular work, the regularization parameters are obtained via weighted-GCV algorithm discussed later in the chapter.

First of all, we need to introduce Tikhonov regularization as an important component of the Lanczos hybrid method that is utilized to solve the minimization problem introduced in equation 1. We take matrix L as the identity matrix and denote the SVD of system matrix A as:

$$A = U\Sigma V^T \quad (45)$$

Where columns u_i of U and v_i of V contain the right and left singular vectors of A, and $\Sigma = \text{diag}(\sigma_1, ..., \sigma_n)$ is a diagonal matrix filled with singular values of A so that $\sigma_1 \geq \sigma_2 \geq \cdots \geq \sigma_n \geq 0$. Now we replace the system matrix with its SVD and get:

$$x_\lambda = \sum_{i=1}^{n} \varphi_i \frac{u_i^T b}{\sigma_i} v_i \quad (46)$$

Where $\varphi_i = \frac{\sigma_i^2}{\sigma_i^2+\lambda^2} \in [0,1]$ is the Tikhonov filter factor [48]. Special care has to be taken in choosing the regularization parameter λ, as over-smoothing will occur if λ chosen is too big, and, correspondedly, under-smoothing will occure if the λ parameter is too small.

In order to optimize the λ parameter, several methods can be employed. In this particular work, we will be utilizing GCV, and its successor weighted-GCV, as the statistics-based methods that do not require prior knowledge of the error magnitude. GCV itself is based on the idea that λ parameter will be helpful in retrieving the missing observations. In GCV, be go through each data value b_j (projection) and optimize λ parameter so that the GCV function presented below will be minimal:

$$G_{A;b}(\lambda) = \frac{n\left\|(I-AA_\lambda^\dagger)b\right\|_2^2}{(trace(I-AA_\lambda^\dagger))^2} \quad (47)$$

Where $A_\lambda^\dagger = (A^TA + \lambda^2 I)^{-1}A^T$ is the pseudo-inverse of $\begin{bmatrix} A \\ \lambda I \end{bmatrix}$ and $x_\lambda = A_\lambda^\dagger b$. We can then replace A with its SVD and utilize standard matlab minimization algorithms.

However, the proposed method only works if the true solution is known and no rounding errors occur that would amount for the information loss. As the regularization parameters are recalculated at each iteration and no known x_{true} exists, we will get better results if the idea of weighted GCV is introduced [46].

In this method, the function described by equation (6) is replaced by:

$$G_{A;b}(\lambda) = \frac{n\left\|(I-AA_{\lambda}^{\dagger})b\right\|_2^2}{(trace(I-\omega AA_{\lambda}^{\dagger}))^2} \quad (48)$$

Where the weighting parameter ω will provide us with smoother ($\omega > 1$) or rougher ($\omega < 1$) solution.The value of ω can be established empirically [49] or with the help of the automated search algorithm [46], the later being utilized in the course of this work.

In the standard GCV method, we methodically work our way through the array by leaving one element at a time – "leave-one-out" method. Leaving the *j*-th element, we try to minimize the prediction error that is described as:

$$\sum_{i=1,i\neq j}^{m}(b_i - [Ax]_i)^2 + \lambda^2\|x\|_2^2 \quad (49)$$

When the *m x m* matrix is defined as:

$$E_j = diag(1,1,\dots 1,0,1,\dots 1) \quad (50)$$

Where 0 corresponds to the *j*-th element, the equation 8 takes form of:

$$\min_x \left\|E_j(b - Ax)\right\|_2^2 + \lambda^2\|x\|_2^2 \quad (51)$$

With the weighted GCV method, instead of 0 we use a weighted coefficient, so that:

$$F_j = diag(1,1,\dots 1,\sqrt{1-\omega},1,\dots 1) \quad (52)$$

And the minimization problem presented in equation 43 becomes:

$$\min_x \left\| F_j(b - Ax) \right\|_2^2 + \lambda^2 \|x\|_2^2 \quad (53)$$

So that the *j*-th observation is still present and not downweighted to zero as is the case when $\omega = 1$ as is in regular GCV. The detailed derivation is presented in [50].

In this case the Tikhonov regularization of the function being minimized changes accordingly. In the standard GCV the trace term can be expressed as:

$$trace\left(I - AA_\lambda^\dagger\right) = \sum_{i=1}^{n} \frac{\lambda^2}{\sigma_i^2 + \lambda^2} + (m - n) \quad (54)$$

While in the weighted GCV function is becomes:

$$trace\left(I - \omega AA_\lambda^\dagger\right) = \sum_{i=1}^{n} \frac{(1-\omega)\sigma_i^2 + \lambda^2}{\sigma_i^2 + \lambda^2} + (m - n) = \sum_{i=1}^{n} (1 - \omega)\varphi_i + \sum_{i=1}^{n} \frac{\lambda^2}{\sigma_i^2 + \lambda^2} + (m - n) \quad (55)$$

Which provides us with the generalized description of the original full system of equations. However, in the described algorithm, the SVD of the whole system matrix A has to be computed simultaneously, which may become impractical at finer resolution. In order to decrease the size of the matrix that has to be operated on simultaneously, we utilize the Lanczos-hybrid method, in particular, Lanczos bidiagonalization (LBD) in combination with Tikhonov regularization as described in [46]. Thus, we obtain a way to solve the large scale ill-posed problem with the limited resources.

The brief description of the method in accordance with [46] is provided below. First, given the system matrix A and sinogram matrix b, we obtain the following decomposition:

$$W^T AY = B \quad (56)$$

Where B is lower bidiagonal matrix, W and Y are orthogonal matrices. The k-th iteration of LBD computes *k*-th column of Y and B and (k+1)-th column of W, so that:

$$A^T W_k = Y_k B_k^T + \alpha_{k+1} y_{k+1} e_{k+1}^T \quad (57)$$

$$AY_k = W_k B_k \quad (58)$$

Where e_{k+1} denotes the last column of the identity matrix of dimensions (k+1), matrices Y_k and W_k have orthonormal columns and the first column of W_k is $b/\|b\|$

This way the least squares problem can be presented as the projected problem:

$$\min_{x \in R(Y_k)} \|b - Ax\|_2 = \min_f \left\| W_k^T b - B_k f \right\|_2 = \min_f \|\beta e_1 - B_k f\|_2 \quad (59)$$

Where $\beta = \|b\|$ and the approximate solution is $x_k = Y_k f$. Each iteration of LBD requires solving the least squares problem. In the ill-conditioned problems, the matrices W_k, Y_k, B_k need to be stored [45].Also, due to the problem being ill-posed, B_k matrix can become very ill-conditioned and an additional regularization is used [51], which can be presented as:

$$f_\lambda = \beta B_{k,\lambda}^{\dagger} e_1 \quad (60)$$

And as dimension of B is very small compared to A, we can store it in the memory and use the direct SVD method to solve for f_λ. We define the SVD of B as:

$$B_k = P_k \begin{bmatrix} \Delta_k \\ 0^T \end{bmatrix} Q_k^T \quad (61)$$

Then the GCV can be defined as:

$$G_{B_k:\beta e_1}(\lambda) = \frac{k \left\| (I - B_k B_{k,\lambda}^{\dagger}) \beta e_1 \right\|_2^2}{(trace(I - B_k B_{k,\lambda}^{\dagger}))^2} = \frac{k\beta^2 (\sum_{i=1}^{n} \left(\frac{\lambda^2}{\delta_i^2 + \lambda^2} [P_k^T e_1]_i \right)^2 + ([P_k^T e_1]_{k+1})^2)}{(1 + \sum_{i=1}^{n} \frac{\lambda^2}{\delta_i^2 + \lambda^2})^2} \quad (62)$$

Where $[P_k^T e_1]_j$ is the j-th component of the $[P_k^T e_1]$, and δ_i is the i-th largest singular value of B_k.

In the case of weighted GCV for bidiagonal systems, formula 52 will be rewritten as:

$$G_{B_k:\beta e_1}(\lambda) = \frac{k\left\|(I-B_kB_{k,\lambda}^{\dagger})\beta e_1\right\|_2^2}{(trace(I-\omega B_kB_{k,\lambda}^{\dagger}))^2} = \frac{k\beta^2(\sum_{i=1}^{n}\left(\frac{\lambda^2}{\delta_i^2+\lambda^2}[P_k^T e_1]_i\right)^2 + ([P_k^T e_1]_{k+1})^2)}{(1+\sum_{i=1}^{n}\frac{(1-\omega)\delta_i^2+\lambda^2}{\delta_i^2+\lambda^2})^2} \quad (63)$$

In order to find ω in adaptive fashion, several assumptions have to be made. First, we assume that little to no regularization is needed to solve the projected LS problem. If $\lambda_{k,opt}$ is the regularization parameter at the k-th iteration, for small k the following expression holds true:

$$0 \leq \lambda_{k,opt} \leq \sigma_{min}(B_k) \quad (64)$$

Where σ_{min} is the smallest singular value of the matrix. Secondly, we assume that with known $\lambda_{k,opt}$ we can express ω as:

$$\frac{\partial}{\partial\lambda}\left(G_{B_k:\beta e_1}(\omega,\lambda)\right)|_{\lambda=\lambda_{k,opt}} = 0 \quad (65)$$

As in reality $\lambda_{k,opt}$ is unknown, for the first iterations that does not yet have ill-conditioning, we are using $\lambda_{k,opt} = \sigma_{min}(B_k)$ to find $\widehat{\omega}_k$, and then for the latter iterations we calculate $\omega_k = mean\{\widehat{\omega}_1, \widehat{\omega}_2, \dots, \widehat{\omega}_k\}$ to find the weighting parameter. It is important to note that as the number of iterations increase the ill-conditioning will start affecting the weighting parameter and $\lambda_{k,opt}$ estimation, so a stopping criteria has to be applied that would determine the finite number of iterations k. In this particular scenario, a certain tolerance threshold for the difference between the two iterations is set. The iterations are terminated when:

$$\left|\frac{\hat{G}(k+1)-\hat{G}(k)}{\hat{G}(1)}\right| < tol \quad (66)$$

And

$$k_0 = \underset{k}{\operatorname{argmin}}\, \hat{G}(k) \quad (67)$$

The implemented reconstruction program based on the algorithm described in this section has been generously provided by Dr. Julianne Chung.

Post-reconstruction, several additional methods can be applied in order to evaluate the resulting images.

Principal component analysis

Obtaining a set of the readings for the photon count at the different energy levels across the x-ray spectra provides us with a series of images that contain the information about the attenuation coefficients at the varying energies. The dependency of the attenuation coefficient from energy is not uniform among the materials and thus observing the attenuation coefficient variation curve can provide an additional information not distinguishable on a single reconstruction slice. However, it requires the person analyzing the x-ray images, such as medical physicist, radiologist or physician, to simultaneously analyze several reconstructed images at a time. However, a unique approach of datamining the spectroscopic images has been developed – Principal Component Analysis (PCA). It allows to display most variance in data through a few derived variables, thus reducing the dimensionality of the data while simultaneously increasing the contrast [52]

Principal component analysis has been first defined in the 19th century by Beltrami and Jordan and since then found its use in various fields including medical imaging [53]. A detailed description of the PCA derivation and application for spectral analysis can be found in [54]. In this particular work, the model proposed by [52] has been utilized.

The algorithm of the PCA analysis can be summarized as:

1) Represent the data in the form of X_{ij}, where i corresponds to the energy window, j corresponds to the individual pixel. In our case i = 1…k, k = 6 (number of energy windows), j = 1… p, p= 65536 (number of pixels)
2) Center each pixels energy value over the average intensity:

   $a_{ij} = x_{ij} - \langle x_j \rangle = x_{ij} - \sum_{i=1}^{k} x_{ij}/k$ (68)

   In this representation, the *j*-th column is the centred energy spectrum for the *j*-th pixel, while the *i*th row of *A* is the centred image $\boldsymbol{a_i}$ atthe *i*-th energy.

3) Find covariance matrix C:

   $C = \frac{1}{k-1} A * A^T$ (69)

4) For C, find eigenvalues and eigenvectors. Eigenvalues should be arranged in decreasing order. Three first eigenvalues and corresponding eigenvectors will serve to encode red, green and blue shades in the image. Let eigenvectors be u_i, i=1..3, then the transformed pixel values are:

   $z_i = u_i^T A = \sum_{l=1}^{k} u_{il} x_l$ (70)

5) As the values of z_i have a mean of zero and variance of corresponding eigenvalue, so before displaying it as a true image we also need to perform scaling for [0 1]:

   $z_i = \frac{z_i - \min(z_i)}{\max(z_i) - \min(z_i)}$ (71)

   The image decoded in RGB standard is then displayed via Matlab inbuilt concatenation function.

RESULTS

Several sets of the experiments performed yielded the following results.

Cross-section calculation modeling

The validity of the model has been checked by comparing the cross-sections generated for the known materials at the established energy (40 keV) with the corresponding values tabulated by Hubbel et al. [32]

The values have been tabulated with the mean error recorded in percentage values. Photoelectric cross-section values are presented in table 1, with the theoretical values obtained from [37]:

Table 1 – Photoelectric cross-section modeling

Element	Theoretical value (Attix), barn/atom	Calculated value, barn/atom	Error, %
Nitrogen (Z = 7)	0.878	0.9115	3.68
Oxygen (Z = 8)	1.64	1.7038	3.74
Aluminum (Z = 13)	15.5	15.7517	1.6
Copper (Z = 29)	480	481.007	0.2
Tin (Z = 50)	3700	3801.9	2.68

As can be observed from Table 1, the error percentage between the experimentally measured values obtained in the literature and the values calculated via the physics' phenomena model presented in this work never reaches beyond 5 %, which is well within the limits defined in the literature [28].

Likewise, the results for the scattering cross-section that combines both the coherent and incoherent scattering are presented in the table 2:

Table 2 – Scattering cross-section modeling

Element	Theoretical value (Attix), barn/atom	Calculated value, barn/atom	Error, %
Nitrogen (Z = 7)	4.44	4.4295	0.2
Oxygen (Z = 8)	5.2	5.2287	0.5
Aluminum (Z = 13)	9.89	9.9149	0.2
Copper (Z = 29)	36.4	36.698	0.8
Tin (Z = 50)	110	110.89	0.8

It should be noted that results for the scattering cross-section modeling are even more aligned with the experimentally obtained results, with the percent error never exceeding 1 %. This effect can be attributed to the nature of the model and the flexibility of the adjustable parameters that take into account the average range of the effective atomic number in question [28]. While it will translate in the necessity for the introduction of the initial guess in the derivation of the scattering cross-section for the unknown atomic number, the advantages of such approach are evident in the precision of the scattering cross-section calculation.

Contrast phantom scan

The contrast phantom scan has been performed in order to establish the validity of the color CT analysis, as well as calculate the effective atomic number of the known materials (water and oil). The image below represents the position of the different materials in the reconstructed slice for the contrast phantom

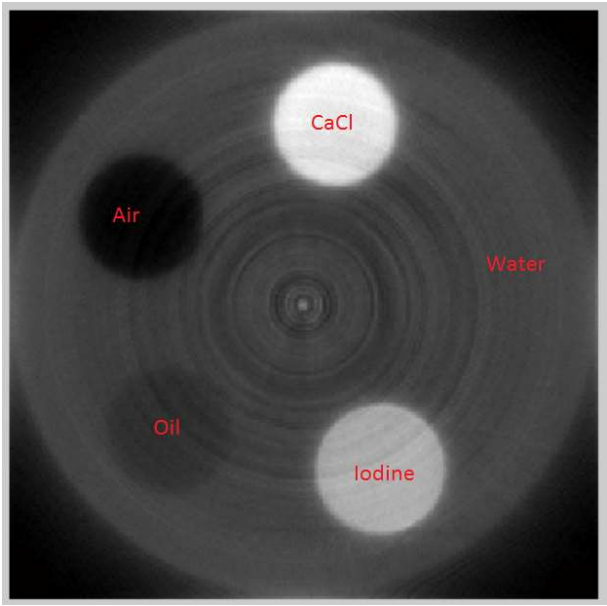

Figure 26 - Contrast phantom slice. Five materials are positioned in the rods, with each material being contrasted against the water-equivalent acrylic tube.

The contrast phantom slices are reconstructed for the 6 energy bins, with mean energies of 22.5, 27.5, 32.5, 37.5, 42.5 and 47.5 keV. The resultant reconstructed images are presented below:

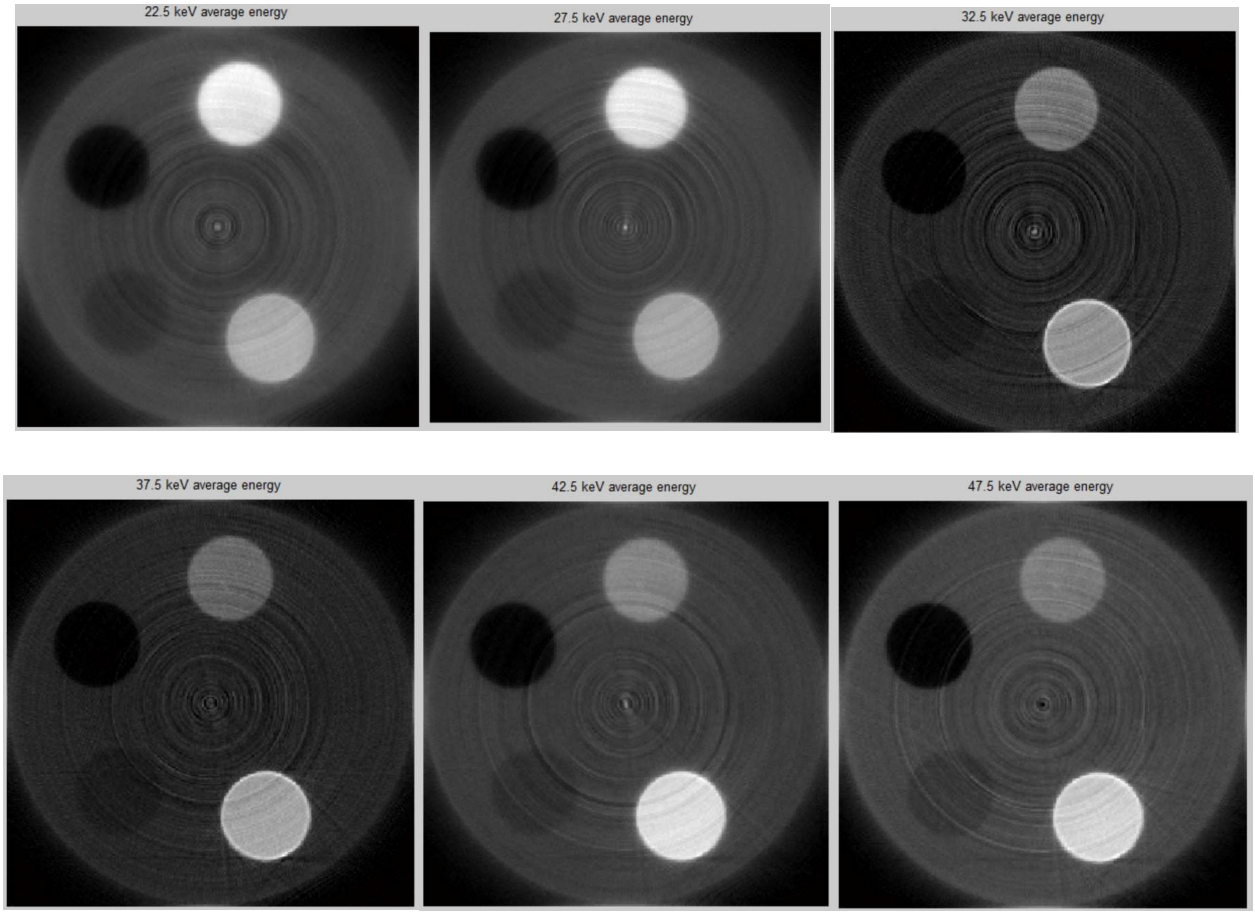

Figure 27 - Contrast phantom reconstructed slices for the various energies. Top left – 20-25 keV energy window; top middle – 25-30 keV energy window; top right – 30-35 keV energy window; bottom left – 35-40 keV energy window; bottom middle – 40-45 keV energy window; bottom right – 45-50 keV energy window

As can be observed from the reconstructed slices, there is a noticeable change in the attenuation coefficient relationship between the calcium chloride powder (bone imitation) and iodine solution (iodine contrast agent imitation). While at the lower energy range calcium chloride is more attenuating and is represented by the more intense shade of white, at the 30-35 energy window the attenuation coefficients of the calcium chloride and iodine solution become equal, and at the higher energy range iodine solution has the higher attenuation range when compared to calcium chloride. Also, is should be noticed that the striking artifacts only become observable for the higher energy range.

After obtaining six slices for the different energy windows, we can proceed with the principal component analysis that combines all six slices within a single image. The resultant image can be found below:

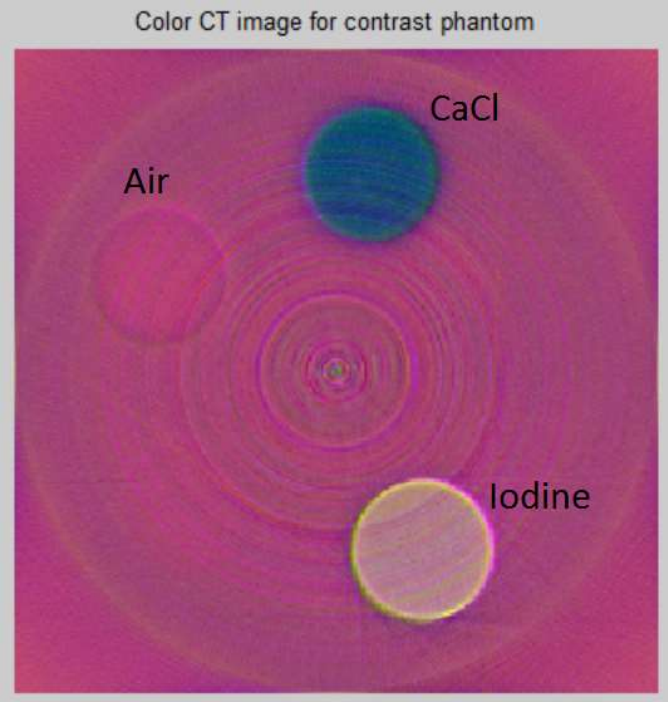

Figure 28 - Contrast phantom color CT image

As can be observed on the contrast phantom color CT image, the differentiation between bone and iodine that might have proved to be challenging in the conventional CT becomes as easy task in the color CT, as the materials comprising the respective slots are vastly different despite having similar attenuation properties.

The attenuation coefficients for water-filled tube are specifically recorded and serve as the calibration point in order to ensure the stability of the reconstruction algorithm. The table of the comparative values is presented below (table 3):

Table 3 – Water linear attenuation coefficients

Average Energy, keV	Reconstructed value, cm^{-1}	Theoretical value (NIST), cm^{-1}
22.5	0.492	5.51E-01
27.5	0.357	3.76E-01
32.5	0.292	2.95E-01
37.5	0.252	2.53E-01
42.5	0.236	2.29E-01
47.5	0.215	2.13E-01

The comparative graphs for the measure and theoretical attenuation coefficients are presented below:

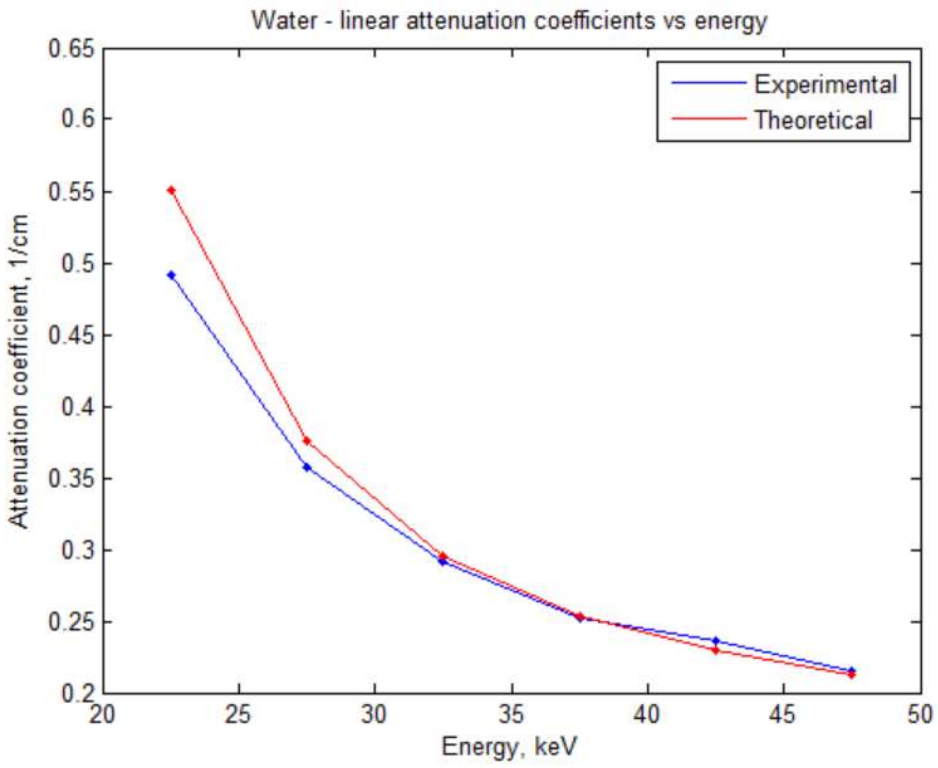

Figure 29 - Water linear attenuation coefficients. Dots correspond to the measured values

As can be notices, the values for the experimentally measured linear attenuation coefficients and the theoretical values provided by the NIST database for the chosen average energy of the corresponding energy window are close. The discrepancy between the values at the lower energy range can be explained by the defects of the detector, as 20-25 keV range approaches the lowest limit of operation [55].

The effective atomic numbers calculated for water are presented in the table below (table 4):

Table 4 – Effective atomic number for water

Energy, keV	Effective atomic number
25 keV	7.2685
30 keV	7.5015
35 keV	7.1474
40 keV	7.9328
45 keV	8.0316
Mean effective atomic number	7.5764

Mean effective atomic number is calculated by finding the average solution for all effective atomic numbers calculated across the energy range. It should be noted that the effective atomic number for water for the diagnostic energy range is 7.53 (Attix, [37]), which corresponds well with the numbers observed in this particular experiment.

In order to establish that the choice of energy pairs the comparison is run for does not significantly affect the effective atomic number, an additional comparison has been run for all energy pairs that have more than 10 keV energy difference:

Table 5 – Variation in the choice of the pairs of μ corresponding to different energies

Energies compared, keV	Z-eff	Energies compared, keV	Z-eff	Energies compared, keV	Z-eff
22-47	7.2308	27-47	7.5772	32-47	7.6193
22-42	7.1355	27-42	7.4920	32-42	7.4849
22-37	6.9873	27-37	7.3478		
22-32	6.9353	22-32			

As can be observed, the variation between the pairs chosen does not significantly affect the effective atomic number.

Next, all of the obtained data is substituted into the linear equation system described by formula 38. The electron density of water utilized in the study is $3.34*10^{29}$ el/m^3 [56]. Solving the system of linear equations that take into account all energies simultaneously yields the following values depending on the number of iterations:

Table 6 – Effective atomic number derived from the system of equations: water

Iteration number	Effective atomic number
1	7.5758
2	6.6768
3	6.7013
4	6.7008

The established threshold value after which the further iterations are stopped is $Z_{i+1} - Z_i < 0.01$. Four iterations are required for the system to reach equilibrium.

As can be seen from the value obtained after the fourth iteration, the calculated effective atomic number is lower than the expected value and lower than the values

calculated by comparing two pairs. This effect can be attributed to the uncertainty introduced by approximation of the non-linear dependency of the linear attenuation coefficient on the effective atomic number by the system of linear equations.

Similarly, experimental values are obtained for the oil-filled tube of the contrast phantom. The attenuation coefficients measured for the oil tube and the corresponding effective atomic numbers are presented in the table below:

Table 7 – Oil attenuation coefficients and effective atomic number

Energy, keV	Linear attenuation coefficient, 1/cm	Effective atomic number
22.5	0.25	5.2664
27.5	0.226	6.4996
32.5	0.191	6.574
37.5	0.202	7.8564
42.5	0.194	8.4426
47.5	0.196	-
Mean EAN		6.9198

According to Brown at al., on average vegetable oil has weighted elemental composition of 0.384 H, 0.581 O and 0.035 C [57], which was used to calculate the theoretical effective atomic number for this energy range, which is 6.89. The theoretical and experimentally obtained values show agreement.

By solving the system of linear equations combining the measurements over the whole spectrum, we obtain the following values over the iterations:

Table 8 - Effective atomic number derived from the system of equations: oil

Iteration number:	Effective atomic number
1	5.5056
2	4.2998
3	4.5713
4	4.5157
5	4.5274
6	4.5249

Once again, it seems that the tendency of the calculated effective atomic number derived by solving the system of linear equations for the whole spectrum to fall within the lower limits of the effective atomic number derived by the comparison of the two neighboring energies is upheld in the case of oil. Oil-equivalent electron density for fat (89% of water electron density) has been utilized in constructing the system of linear equations [58].

The reconstructed slices for the iodine contrast phantom

The conventional CT image for the water iohexol solution of the varying concentration is presented on the following figure:

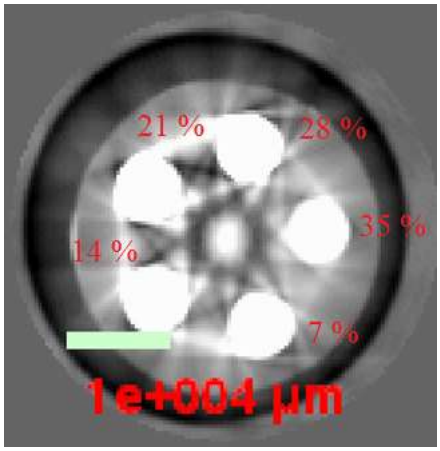

Figure 30 - Conventional CT image of the iodine contrast phantom

As can be seen, little to no contrast difference in the image brightness for the different concentrations of iodine is present on the reconstructed slice above. In addition, the striking artifact is significant and causes the noticeable brightness/contrast distortion in the water-equivalent filled regions that are supposed to have uniform attenuation. The aforementioned facts lead us to the conclusion that the conventional CT is ill suited for detecting the subtle differences in the iodine contrast agent concentration variability.

Instead, the energy-discriminative CT is performed and nine imaging slices are constructed for the same object. Each slice is reconstructed from the photons that belong to the narrow energy range, with photons with the energy from 20 keV to 65 keV being covered. The overall layout of the iodine contrast agent phantom is presented as:

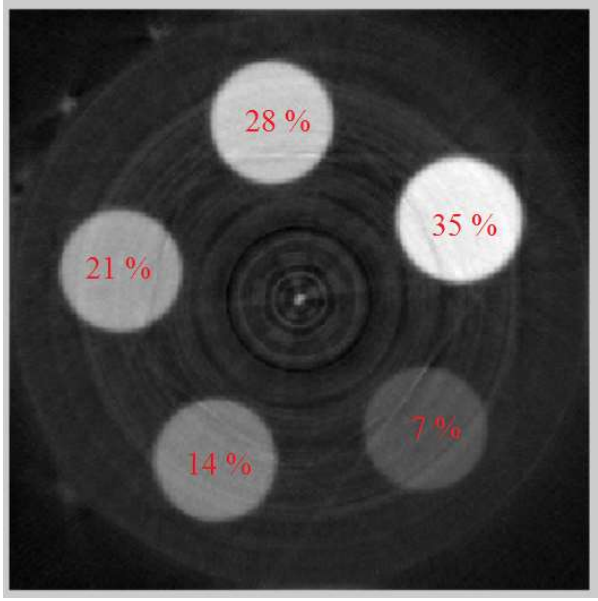

Figure 31 - The layout of the tubes filled with the solutions with the different concentration of iodine

The image above presents a reconstructed slice for only a narrow (60-65 keV) energy range. As can be seen, the differentiation between various concentrations of iodine becomes a much easier task with the energy-discriminative detector in comparison to the conventional CT.

The reconstructed slices for all energy bin covering 20-65 keV are presented below:

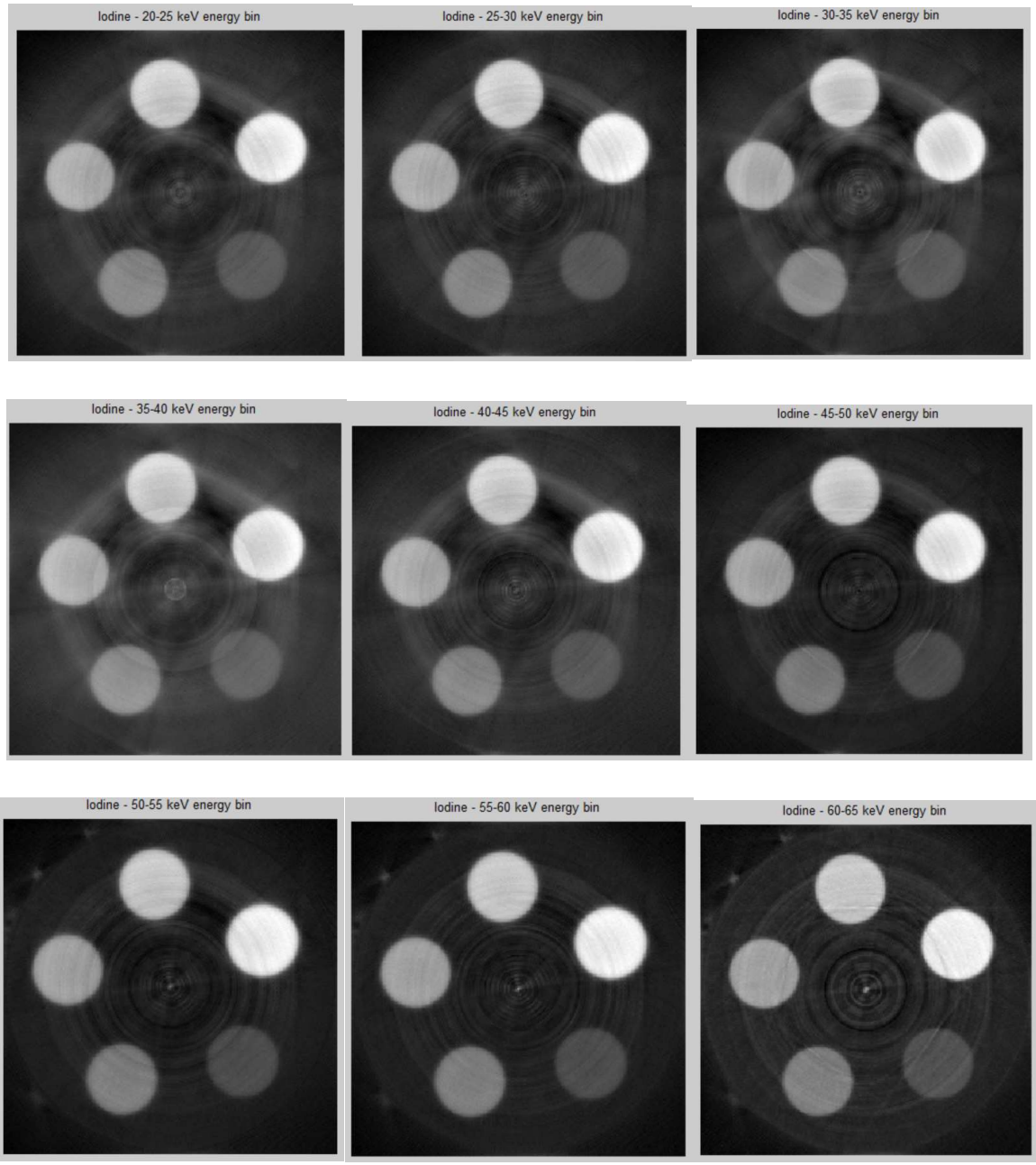

Figure 32 - Iodine contrast phantom with varying concentrations for different energy bins. The reconstructed slice corresponds to the readings for the photons with: top left – 20-25 keV energy; top middle – 25-30 keV energy; top right – 30-35 keV energy; middle left – 35-40 keV energy; middle – 40-45 keV energy; middle right – 45-50 keV energy; bottom left – 50-55 keV energy; bottom middle – 55-60 keV energy; bottom right – 60-65 keV energy

As can be seen of the figure 32, the clear contrast between the solutions with different concentrations of iodine persist across the whole energy spectrum. In addition, it should be noted that the presence of the striking artifacts is less pronounced in the case of the color CT, although distinguishing between water and air becomes more difficult at the lower energies, probably due to the additional scattering effects introduced by the k-edge. Combined together, the nine slices corresponding to the different parts of the spectrum can form a single color CT image presented below:

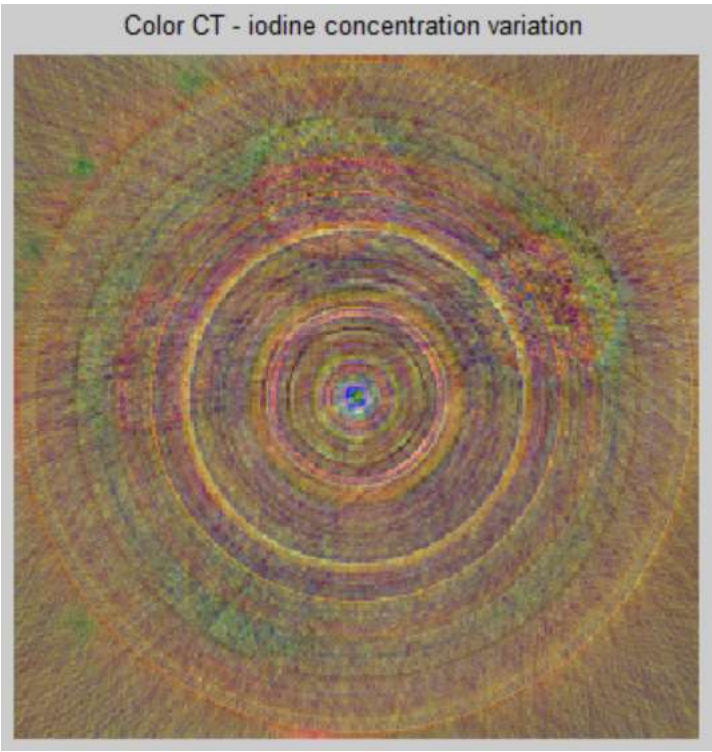

Figure 33 - Color CT for the iodine phantom

As can be observed from the color CT for iodine contrast agent comparison, the differentiation between the different concentrations of iodine, as well as the differentiation between the iodine and surrounding tissue-equivalent acrylic material becomes even worse than was the case with the conventional CT. The material differentiation that was superb for the iodine vs calcium chloride demonstrated in the

figure 28 is absent with the different concentrations of the iodine. This leads to the conclusion that while the usage of the narrow energy window for the data acquisition is highly beneficial in terms of iodine contrast agent differentiation for the conventional grey-scale imaging, the color RGB imaging that would combine the readings from nine energy bins is impractical in the case of the iodine contrast agent concentration differentiation. Therefore, other methods have to be employed.

The effective atomic number differentiation for the different concentrations of the iodine contrast agent iohexol

The effective atomic number differentiation might provide for a better iodine contrast agent's concentration differentiation. Due to the complexity of calculating the effective atomic number of the solution based on the linear attenuation coefficient experimentally measured for that solution, several techniques are employed. First, we establish the baseline effective atomic number for the known averaged solution of iohexol and water [18], with the known mass attenuation coefficients and atomic cross-sections derived from the NIST database. The comparative chart for the effective atomic numbers of the different concentrations of the iodine contrast agent for semi-known solution is presented below:

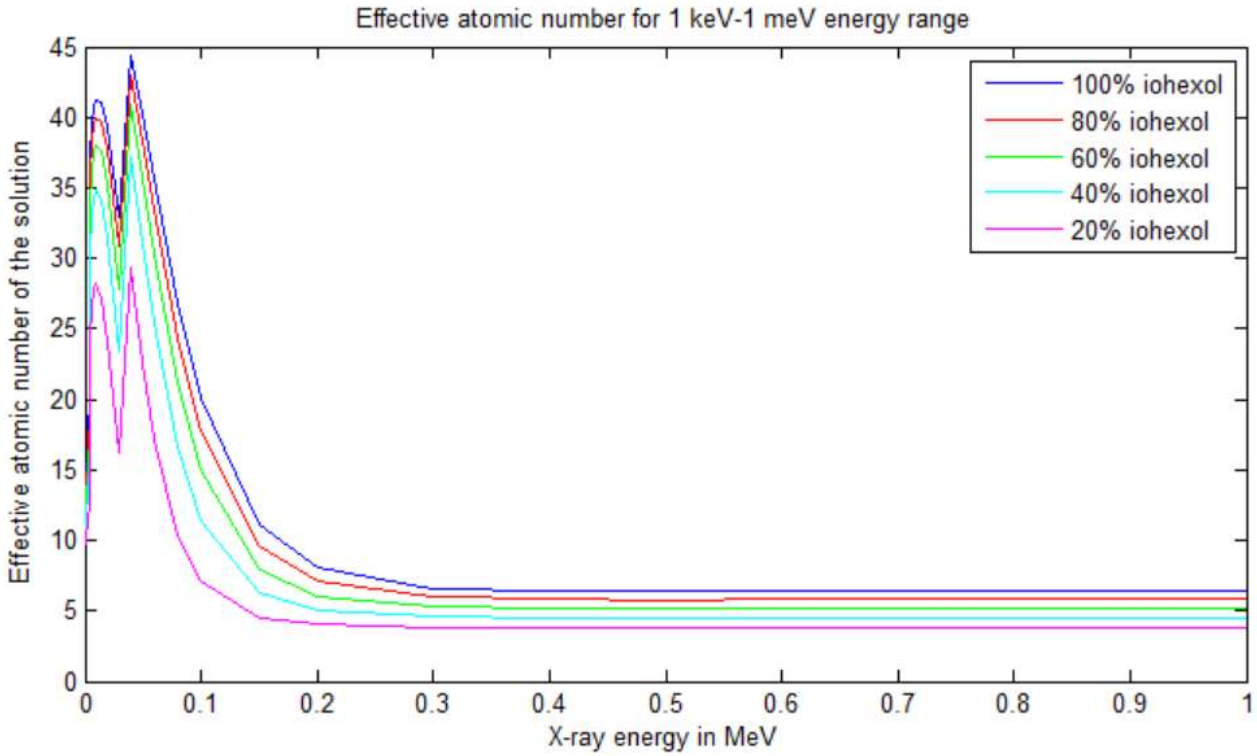

Figure 34 - Effective atomic number for the iohexol-water solution for the energy range of 1 keV – 1 meV

As can be seen from the graph above, there is a difference in the effective atomic number is the most pronounced at the lower energy range (<20 keV) and in the upper diagnostic energy range (80-120 keV), while the effective atomic numbers in the mid-diagnostic energy range (20-70 keV) are largely affected by the presence of the k-edge. The graph above considers the solution of pure iohexol and distilled water. It should be noted that the lowest concentration of iohexol also presented the most deviating effective atomic numbers, making it easier to identify the lowest concentration of iohexol (20%) in comparison to higher concentrations (40, 60, 80 and 100%).

These results present the ideal case scenario with the known exact atomic composition of the solution, and mass attenuation coefficients measures for the ideal detector, with no collimation or filtering. However, such is not the case in the real life. The measurements taken for the linear attenuation coefficients for the Omnipaque

solution diluted by water include additional components of the contrast agent solution, as well as the presence of the filters, scattering introduced by the x-ray tube case, collimators, filters et.c. Therefore, the results derived from the experimental data will only roughly match the results calculated by the prediction model presented above.

Table 9 – Mean linear attenuation coefficients measures for the iodine contrast agent of the varying concentrations

	7% iodine, μ per mm	14% iodine, μ per mm	21% iodine, μ per mm	28% iodine, μ per mm	35% iodine, μ per mm
20-25 keV	0.1081	0.1786	0.2389	0.2925	0.3316
25-30 keV	0.0983	0.1638	0.2229	0.2747	0.3132
30-35 keV	0.1081	0.1786	0.2387	0.2912	0.325
35-40 keV	0.1165	0.1986	0.2624	0.317	0.3516
40-45 keV	0.1077	0.1885	0.2557	0.3145	0.3566
45-50 keV	0.0885	0.1579	0.2217	0.2825	0.3268
50-55 keV	0.0856	0.1541	0.2014	0.2553	0.3061
55-60 keV	0.077	0.1365	0.1787	0.2286	0.2755
60-65 keV	0.0701	0.1193	0.1539	0.1961	0.2362

The corresponding graph for the various linear attenuation coefficients measured is provided below:

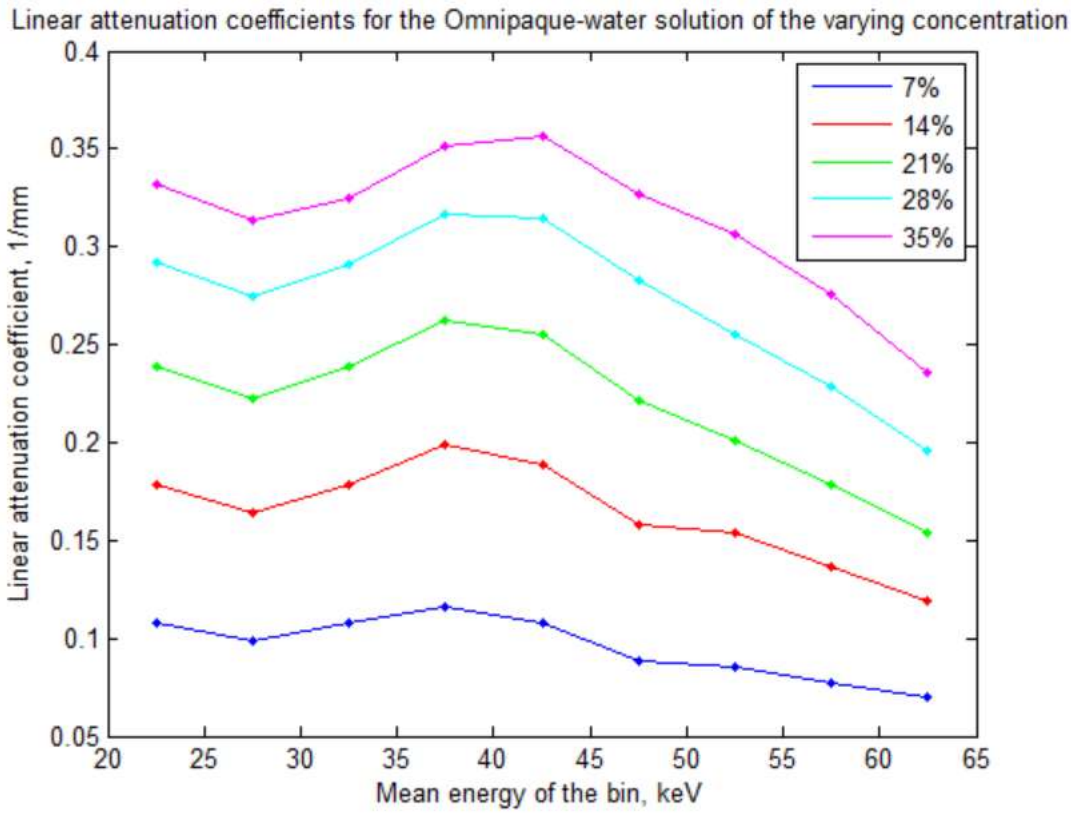

Figure 35 - Linear attenuation coefficients for the contrast agents of the varying concentrations

The effective atomic numbers are calculated for every energy bin do that the variability can be recorded across the whole range of the 70 keV x-ray cone beam spectrum.

The results can be presented as:

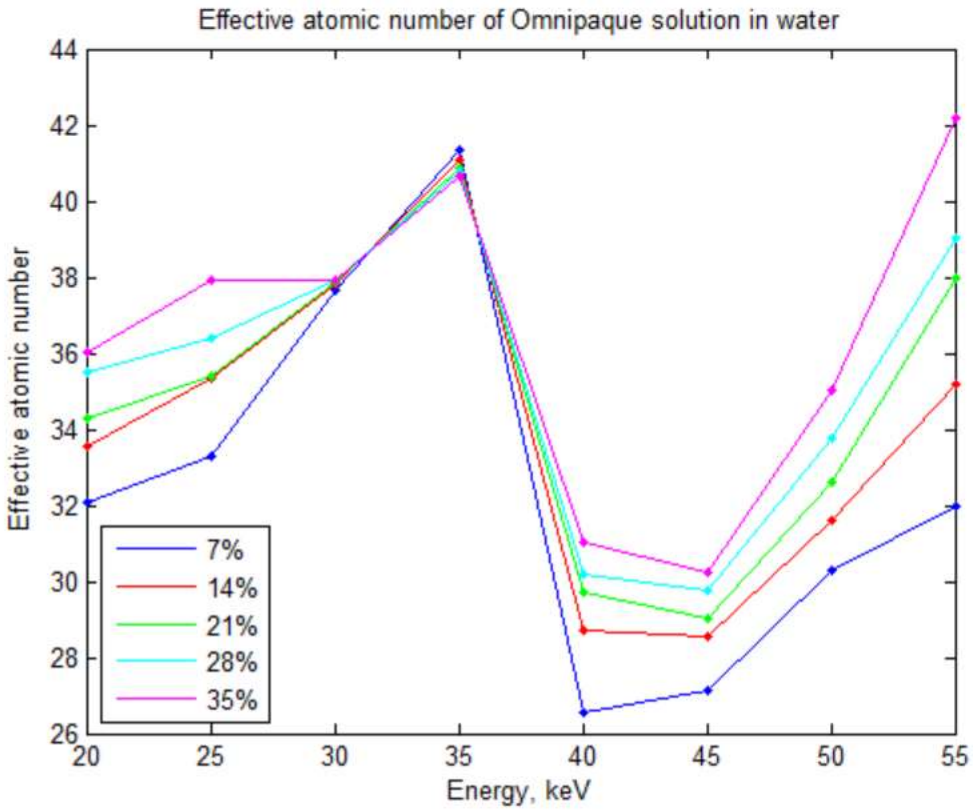

Figure 36 - Effective atomic numbers depending on energy

As can be noticed from the graph above, the k-edge has a significant effect on the effective atomic numbers of the iohexol solutions of different concentrations, with the numbers overlapping each other in the region from 30 to 45 keV, which can be attributed to the gradual nature of the iodine k-edge, as well as inbuilt uncertainty of the detector with the threshold values having a ±2.5 keV uncertainty.

Likewise, an attempt to find the solution for the spectrum of measured energies has been made via the linear equation system. Only the readings for 47.5 keV, 52.5 keV, 57.5 keV and 62.5 keV have been utilized in order to avoid the k-edge contamination and inbuilt detector uncertainty at the energy range of 20-25 keV. The electron density of the iohexol was calculated based on the pharmaceutic specifications

[59][60]. The overall density of the solution is calculated as the proportion of water vs Omnipaque. The results are presented in the table:

Table 10 - Effective atomic number derived from the system of equations: iodine solution

Iteration number	7 %	14 %	21 %	28 %	35 %
1	19.3589	24.0274	26.6788	30.4094	32.3126
2	18.5323	23.4050	26.4327	29.4746	31.7137
3	18.4438	23.3015	26.3863	29.2842	31.5810
4	18.4341	23.2841	26.3776	29.2454	31.5517
5	-	23.2811	-	29.2374	31.5453

As can be seen from this table, the calculated effective atomic numbers are significantly below the effective atomic numbers calculated via the dual-energy approach for the neighboring energies. However, the contrast between the effective atomic numbers for the solutions of the varying concentrations provided by the spectrum approach is much more pronounced.

DISCUSSION AND CONCLUSION

The study of the capabilities of energy discriminative color-coded computer tomography validated the previously established methods. The validity of the measurements reconstructed from the data derived from the color CT system has been determined by comparing the attenuation coefficient for the water with the values presented in literature. Several additional experiments have been performed in order to determine the capabilities of the color CT, including the scanning of the contrast phantom containing different materials with attenuation properties approximating those found in human body. The principal component analysis method has been implemented in order to synthesize a single reconstructed image from the slices reconstructed from the data obtained for different energy windows that comprise the overall x-ray beam spectrum. The particular contrast between the bone-imitating calcium chloride powder and 5% iodine solution, while being hard to interpret on the traditional gray-scale CT, has been especially pronounced on the synthesized color CT slice that included the information across the whole spectrum of the x-ray beam.

The study of the effective atomic numbers of the water and oil has established the validity of the method, as well as provided an insight in the potential new patterns observed by comparing the values derived for the effective atomic number by comparing neighboring energy readings vs comparing the energy values with bigger difference. The mean value for the overall spectrum has been calculated. An important insight has been obtained by comparing the average effective atomic number calculated as the mean value of the series of comparisons between the two neighboring values, and solving the system of equations that took into account all attenuation coefficients recorded for different energy values simultaneously.

The study of the effective atomic numbers of the iohexol contrast agent of different concentration dissolved in the water approximation of the natural blood solution was performed. The traditional gray-scale CT, as well as previously discussed PCA-based color CT, have not yielded satisfactory results, leading to necessity to investigate the potential of the z-effective imaging for iohexol. We observed the specific effect the k-edge of the iodine (33 keV) on the effective atomic number variation as derived from the attenuation coefficient readings for the corresponding energies at the 20-65 keV energy range. The resultant low variation in the effective atomic numbers of the iohexol solution of different concentration was explained by the k-edge strong influence. The approximate nature of the energy bin thresholds attributed to the detector in-built uncertainties was speculated to be a contributing factor. An interesting result was demonstrated by calculating a single effective atomic number for the compound by solving the system of linear equations that would only take into account readings for the energies of 45-65 keV. While the values derived by this method were lower than the values calculated by the step-by-step comparison of the effective atomic numbers derived for the neighboring energies, the overall contrast demonstrated was much better. That opens a discussion of the suitability of the method in enhancing the contrast with the necessity for adjustment of the recorded value to the physical constant derived from the literature by a certain offset.

Alternatively, new venues for the research might be introduced by investigating the materials with the k-edge that is significantly different from the range of the meaningful readings as obtained by the detector. One such alternative might be gold, with k-edge ≈80 keV being above the readings of 20-65 keV utilized in this study. The advance research in the use of gold nanoparticles makes it an attractive venue.

Another possible material used for the effective atomic number imaging is calcium. Contrary to gold, calcium k-edge is far below 20 keV, making it another attractive target material. The deposits of calcium are often associated with the build-

up of plaques that characterize the atherosclerotic disease. On the other hand, microcalcinates found in the breast tissue of females are often an early marker of the developing breast cancer. With both diseases being on the rise, the investigating of the method of detecting calcium deposits in the tissue by tracking the effective atomic number variation might prove a powerful diagnostic tool that would make it possible to omit the use of contrast agent altogether.

The principles of the effective atomic number imaging might not only be applicable in the biomedical imaging, but also in security screening in the airports and other places with high security risks. The capability of the z-effective imaging to be targeted towards certain materials can be geared towards detecting the chemical compounds associated with explosives. Likewise, the method can be applied for industrial screening, making for a useful tool in detecting caverns and defects. Overall, the method is versatile enough to find a wide range of application within the fields that use x-ray.

All of that leads to the conclusion that further investigation of the effective atomic number variation depending on the energy in the energy-discriminative computer tomography is a promising venue of research.

REFERENCES

1) Shilo, Malka, et al. "Nanoparticles as computed tomography contrast agents: current status and future perspectives." Nanomedicine 7.2 (2012): 257-269

2) Ghaghada KB, Badea CT, Karumbaiah L et al. Evaluation of tumor microenvironment in an animal model using a nanoparticle contrast agent in computed tomography imaging. Acad. Radiol.18(1),20–30 (2011)

3) Aillon KL, El-Gendy N, Dennis C, Norenberg JP, Mcdonald J, Berkland C. Iodinated nano clusters as an inhaled computed tomography contrast agent for lung visualization. Molecular Pharm.7(4),1274–1282 (2010)

4) Hyafil F, Cornily J-C, Feig JE et al. Noninvasive detection of macrophages using a nanoparticulate contrast agent for computed tomography. Nat. Med.13(5),636–641 (2007).

5) Christiansen C. X-ray contrast media: an overview. Toxicology, 2005;209(2):185-187

6) Dean JA, ed. Lange's Handbook of Chemistry. 14th ed. NewYork, NY: McGraw Hill; 1992:4.18

7) Pasternak, Jeffrey J., and Eric E. Williamson. "Clinical pharmacology, uses, and adverse reactions of iodinated contrast agents: a primer for the non-radiologist." Mayo Clinic Proceedings. Vol. 87. No. 4. Elsevier, 2012

8) Cademartiri F, Mollet NR, van der Lugt A, et al. Intravenous contrast material administration at helical 16-detector row CT coronary angiography: effect of iodine concentration on vascular attenuation. Radiology 2005;236:661-665

9) Yanaga Y, Awai K, Nakayama Y, et al. Optimal dose and injection duration (injection rate) of contrastmaterial for depiction of hypervascular hepatocellular carcinomas by multidetector CT. Radiat Med 2007;25:278-288.

10) Behrendt FF, Mahnken AH, Stanzel S, et al. Intraindividual comparison of contrast media concentrations for combined abdominal and thoracic MDCT. AJR Am J Roentgenol 2008;191:145-150.

11) Bae KT. Peak contrast enhancement in CT and MR angiography: when does it occur and why? Pharmacokinetic study in a porcine model. Radiology 2003;227:809-816.

12) Jo, Byoung Goo, et al. "Comparison of enhancement and image quality: different iodine concentrations for liver on 128-slice multidetector computed tomography in the same chronic liver disease patients." The Korean journal of internal medicine 31.3 (2016): 461.

13) https://en.wikipedia.org/wiki/Effective_atomic_number

14) Segre, E. , Experimental Nuclear Physics, Vol. 1 (John Wiley, 1953)

15) Murty, R. C. "Effective atomic numbers of heterogeneous materials." (1965): 398-399

16) Hine, G. E. , Nucleonics, 10, 9 (1952). | ISI | ChemPort |

17) Glasser, O. , Physical Foundations of Radiology (Harper, 1947)

18) Manohara, S. R., et al. "On the effective atomic number and electron density: a comprehensive set of formulas for all types of materials and energies above 1keV." Nuclear Instruments and Methods in Physics Research Section B: Beam Interactions with Materials and Atoms 266.18 (2008): 3906-3912

19) Taylor, M. L., et al. "Robust calculation of effective atomic numbers: The Auto-Zeff software." Medical physics 39.4 (2012): 1769-1778.

20) G. N. Hounsfield, “Computerized transverse axial scanning tomography: Part 1. Description of system,” Br. J. Radiol. 46, 1016–1022, 1973

21) Gorshkov, Vjacheslav. "The effective atomic number and the mass attenuation coefficient of a multicomponent object for the continuous spectrum of the radiation." Nondestructive Testing and Evaluation (2016): 1-11.

22) Alves, H., I. Lima, and R. T. Lopes. "Methodology for attainment of density and effective atomic number through dual energy technique using microtomographic images." Applied Radiation and Isotopes 89 (2014): 6-12

23) Garcia, Luis Isaac Ramos, José Fernando Pérez Azorin, and Julio F. Almansa. "A new method to measure electron density and effective atomic number using dual-energy CT images." Physics in medicine and biology 61.1 (2015): 265

24) Tsunoo, T., et al. "Measurement of electron density and effective atomic number using dual-energy x-ray CT." Nuclear Science Symposium Conference Record, 2004 IEEE. Vol. 6. IEEE, 2004.

25) Zou, Wenjuan, et al. "Atomic number and electron density measurement using a conventional x-ray tube and a cdte detector." Japanese journal of applied physics 47.9R (2008): 7317

26) Torikoshi, Masami, et al. "Design of synchrotron light source and its beamline dedicated to dual-energy x-ray computed tomography." journal of Biomedical Optics 6.3 (2001): 371-377

27) J.H. Lambert, Photometria sive de mensura et gradibus luminis, colorum et umbrae: Photometry, or, On the measure and gradations of light, colors, and shade] (Augsburg ("Augusta Vindelicorum"), Germany: Eberhardt Klett, 1760); Beer (1852)

"Bestimmung der Absorption des rothen Lichts in farbigen Flüssigkeiten" (Determination of the absorption of red light in colored liquids), Annalen der Physik und Chemie, vol. 86, pp. 78–88

28) D. F. Jackson and D. J. Hawkes, ‘‘X-Ray attenuation coefficients of elements and mixtures,’’ Phys. Rep. 70, 169–233, 1981.

29) http://en.wikibooks.org/wiki/Basic_Physics_of_Digital_Radiography/The_Patient

30) Einstein A., Concerning an Heuristic Point of View Toward the Emission and Transformation of Light. Annalen der Physik 17 (1905): 132-148

31) W. Heitler, The Quantum Theory of Radiation (Oxford University Press, 3rd ed. 1954)

32) Hubbell, J. H., et al. "Atomic form factors, incoherent scattering functions, and photon scattering cross sections." Journal of physical and chemical reference data 4.3 (1975): 471-538

33) HA Bethe, EE Salpeter; Quantum Mechanics of One and Two Electron Atoms. Springer-Verlag, Berlin (1957)

34) Stobbe, Martin. "Zur quantenmechanik photoelektrischer prozesse." Annalen der Physik 399.6 (1930): 661-715

35) Sauter, Fritz. "Über das Verhalten eines Elektrons im homogenen elektrischen Feld nach der relativistischen Theorie Diracs." Zeitschrift für Physik 69.11-12 (1931): 742-764

36) Documentation, Matlab. "The MathWorks Inc." (2005)

37) Attix, Frank Herbert. Introduction to radiological physics and radiation dosimetry. John Wiley & Sons, 2008

38) Mott, Nevill Francis, and Harrie Stewart Wilson Massey. "The theory of atomic collisions." The theory of atomic collisions, by Mott, NF; Massey, Harrie Stewart Wilson. Oxford, Clarendon Press, 1949. 1 (1949)

39) By Kieranmaher - Own work, Public Domain, https://commons.wikimedia.org/w/index.php?curid=12719582

40) Klein, O; Nishina, Y (1929). "Über die Streuung von Strahlung durch freie Elektronen nach der neuen relativistischen Quantendynamik von Dirac". Z. Phys. 52 (11-12): 853 and 869

41) Powell, M. J. D., "A Fortran Subroutine for Solving Systems of Nonlinear Algebraic Equations," Numerical Methods for Nonlinear Algebraic Equations, P. Rabinowitz, ed., Ch.7, 1970

42) Noo, Frédéric, et al. "Analytic method based on identification of ellipse parameters for scanner calibration in cone-beam tomography." Physics in medicine and biology 45.11 (2000): 3489.

43) Siddon, Robert L. "Fast calculation of the exact radiological path for a three-dimensional CT array." Medical physics 12.2 (1985): 252-255

44) Groetsch, C. W. "The Theory of Tikhonov Regularization for Fredholm Integral Equations of the First Kind (Boston, MA: Pitman)." (1984).

45) Paige, Christopher C., and Michael A. Saunders. "LSQR: An algorithm for sparse linear equations and sparse least squares." ACM Transactions on Mathematical Software (TOMS) 8.1 (1982): 43-71.

46) Chung, Julianne, James G. Nagy, and DIANNE P. O'Leary. "A weighted GCV method for Lanczos hybrid regularization." Electronic Transactions on Numerical Analysis 28 (2008): 149-167.

47) Björck, Åke. "A bidiagonalization algorithm for solving large and sparse ill-posed systems of linear equations." BIT Numerical Mathematics 28.3 (1988): 659-670.

48) Hansen, Per Christian. Rank-deficient and discrete ill-posed problems. Lyngby: Polyteknisk Forlag, 1996

49) Y. Kim and C. Gu, Smoothing spline Gaussian regression: More scalable computation via efficient approximation, J. Roy. Stat. Soc., 66 (2004), pp. 337-356

50) G. H. Golub, M. Heath, and G. Wahba, Generalized cross-validation as a method for choosing a good ridge parameter, Technometrics, 21 (1979), pp. 215-223

51) G. H. Golub, F. T. Luk, and M. L. Overton, A block Lanczos method for computing the singular values and corresponding singular vectors of a matrix, ACM Trans. Math Soft.,7 (1981), pp. 149-169.

52) Butzer, J. S., et al. "Medipix imaging-evaluation of datasets with PCA." Image and Vision Computing New Zealand, 2008. IVCNZ 2008. 23rd International Conference. IEEE, 2008

53) I. Jollife, Principal Component Analysis, 2nd ed. Springer-Verlag, 2002.

54) A. R. Kalukin, M. Van Geet, and R. Swennen, “Principal component analysis of multienergy x-ray computed tomography of mineral samples,” IEEE Transactions on Nuclear Science, vol. 47, no. 5, pp. 1729–1736, Oct. 2000.

55) http://www.evproducts.com/evaluator3500.html

56) Hall, G. G., and C. M. Smith. "The electron density of the water molecule." *Theoretica chimica acta* 69.1 (1986): 71-81.

57) Brown, Saxby, et al. "Investigation of the relationship between linear attenuation coefficients and CT Hounsfield units using radionuclides for SPECT." Applied Radiation and Isotopes 66.9 (2008): 1206-1212

58) Saito, A. I., et al. "2831: Accurate Heterogeneous Dose Calculation for Lung Cancer Patients Without High Resolution CT Densities." *International Journal of Radiation Oncology* Biology* Physics* 66.3 (2006): S677-S678.

59) http://www.chemicalbook.com/ProductMSDSDetailCB2262877_EN.htm

60) Kalef-Ezra, J. A., et al. "Electron density of tissues and breast cancer radiotherapy: a quantitative CT study." *International Journal of Radiation Oncology* Biology* Physics* 41.5 (1998): 1209-1214.

APPENDICES

Appendix A

Table A1 – Screening factor N(Z)

Z (element)	N(Z)	Z (element)	N(Z)
1	0.5	28	1.0739
2	0.7358	29	1.0758
3	0.8694	30	1.0791
4	0.9197	31	1.0822
5	0.9547	32	1.0854
6	0.9615	33	1.0882
7	0.9722	34	1.0912
8	0.9798	35	1.0931
9	0.9856	36	1.097
10	0.9901	37	1.1001
11	0.9979	38	1.1003
12	1.0075	39	1.1062
13	1.0133	40	1.1089
14	1.0199	41	1.112
15	1.0249	42	1.1151
16	1.0303	43	1.1182
17	1.0348	44	1.1209
18	1.039	45	1.1235
19	1.0436	46	1.126
20	1.0484	47	1.1297
21	1.052	48	1.1331
22	1.0556	49	1.1361
23	1.0591	50	1.1389
24	1.0614	51	1.1417
25	1.0653	52	1.1445
26	1.0682	53	1.1471
27	1.071	54	1.1495

Appendix B

Table B1 – Atomic form factor F(x,Z)

x\Z	H	He	Li	Be	B	C
0	1	2	3	4	5	6
0.005	0.9945	1.9995	2.9966	3.997	4.9971	5.9974
0.01	0.9779	1.9982	2.9865	3.988	4.9885	5.9898
0.015	0.9504	1.996	2.9699	3.9732	4.9742	5.9771
0.02	0.9921	1.993	2.9472	3.9525	4.9542	5.9594
0.025	0.98632	1.9891	2.919	3.9264	4.9289	5.9368
0.03	0.98039	1.9844	2.885	3.8947	4.8981	5.9093
0.04	0.96554	1.9724	2.8044	3.8168	4.8217	5.8406
0.05	0.94693	1.9569	2.7106	3.7215	4.727	5.7544
0.07	0.89987	1.9169	2.5071	3.4924	4.4934	5.5369
0.09	0.84238	1.866	2.309	3.2325	4.2189	5.2702
0.1	0.81082	1.8364	2.219	3.0976	4.068	5.1225
0.125	0.72711	1.7551	2.0358	2.7844	3.7006	4.7407
0.15	0.64129	1.6612	1.906	2.4921	3.328	4.331
0.175	0.55811	1.5603	1.8184	2.2629	2.9974	3.9371
0.2	0.48078	1.4585	1.7425	2.0771	2.7113	3.5775
0.25	0.34974	1.2522	1.6258	1.8354	2.2731	2.9614
0.3	0.25127	1.0586	1.5115	1.6951	1.9863	2.5015
0.4	0.13044	0.73794	1.2688	1.5195	1.6831	1.9512
0.5	0.070592	0.50953	1.0313	1.3603	1.5262	1.6856
0.6	0.040325	0.35416	0.8255	1.193	1.4003	1.5353
0.7	0.024285	0.24952	0.65	1.0277	1.2741	1.4245
0.8	0.015335	0.1786	0.5123	0.8743	1.1454	1.3206
0.9	0.010091	0.12995	0.40437	0.73812	1.0187	1.2165
1	0.0068811	0.09612	0.32046	0.6206	0.89873	1.1121
1.25	0.0029947	0.0484	0.18375	0.42798	0.64332	0.86482
1.5	0.0014937	0.02651	0.1102	0.26235	0.45565	0.65662

2	0.0004890 3	0.00964	0.04481	0.11982	0.23265	0.37202
2.5	0.0002035 3	0.0041962	0.020891	0.059945	0.12506	0.21465
3	0.0000990 16	0.0020934	0.01092	0.03272	0.07154	0.12882
3.5	0.0000537 3	0.0011537	0.0061907	0.019085	0.043127	0.080452
4	0.0000316 04	0.00068559	0.0037383	0.01181	0.02732	0.05223
5	0.0000129 97	0.00028543	0.0015869	0.0051521	0.01231	0.02433
6	6.2819E-06	0.0001389	0.00078063	0.0025717	0.00627	0.01265
7	3.3953E-06	0.00007539 8	0.00042656	0.001418	0.0034963	0.0071471
8	0.0000019 92	0.00004436 3	0.00025209	0.00084309	0.0020943	0.0043194
10	8.1675E-07	0.00001825 6	0.0001043	0.00035136	0.00088081	0.0018364
15	1.615E-07	3.6259E-06	0.00002083 5	0.00007073 8	0.00017906	0.00037767
20	5.1116E-08	0.00000150 5	6.6279E-06	0.00002257 5	0.00005737 3	0.00012157
50	1.3091E-09	2.9749E-08	1.7245E-07	5.9153E-07	1.5152E-06	3.2386E-06
80	1.9976E-10	4.578E-09	2.6652E-08	9.1828E-08	2.3627E-07	5.0734E-07
100	8.1822E-11	1.8855E-09	1.1007E-08	3.8027E-08	9.8106E-08	2.1123E-07
1000	8.1823E-15	2.3461E-13	1.4995E-12	5.6197E-12	1.5611E-11	3.5964E-11

1000000	8.1823E-27	5.1312E-23	4.4404E-22	2.0249E-21	6.4746E-21	1.6609E-20
1000000000	8.1823E-39	5.1205E-32	4.4444E-31	2.0332E-30	6.5261E-30	1.681E-29
x\Z	N	O	F	Ne	Na	Mg
0	7	8	9	10	11	12
0.005	6.9938	7.9974	8.9976	9.9978	10.989	11.991
0.01	6.987	7.9912	8.9919	9.9926	10.975	11.975
0.015	6.9793	7.9814	8.9831	9.9845	10.956	11.951
0.02	6.9633	7.9669	8.9699	9.9724	10.922	11.914
0.025	6.9428	7.9484	8.9531	9.957	10.88	11.867
0.03	6.9179	7.9259	8.9326	9.9382	10.829	11.811
0.04	6.8553	7.8692	8.8808	9.8906	10.709	11.673
0.05	6.776	7.7974	8.815	9.83	10.573	11.505
0.07	6.5741	7.6117	8.6441	9.6719	10.248	11.114
0.09	6.3217	7.3767	8.4255	9.4682	9.9188	10.685
0.1	6.1844	7.2441	8.3011	9.3515	9.9756	10.454
0.125	5.7961	6.8748	7.9501	9.0193	9.3796	9.9571
0.15	5.3873	6.4698	7.5579	8.6427	9.0209	9.4723
0.175	4.9692	6.0466	7.1384	8.233	8.6804	9.0948
0.2	4.5604	5.6197	6.7056	7.8031	8.3376	8.7133
0.25	3.8251	4.8047	5.8475	6.9254	7.6159	8.0746
0.3	3.2184	4.0858	5.0499	6.0764	6.8774	7.4307
0.4	2.3939	3.0031	3.755	4.6139	5.4647	6.1879
0.5	1.9378	2.3351	2.8701	3.531	4.289	5.0315
0.6	1.6948	1.9445	2.3062	2.7864	3.3942	4.0519
0.7	1.5522	1.7132	1.9546	2.2929	2.7488	3.2864
0.8	1.4464	1.5667	1.7326	1.9688	2.2994	2.7203
0.9	1.3521	1.4623	1.586	1.754	1.9924	2.3132
1	1.262	1.3763	1.481	1.6073	1.7819	2.0213

1.25	1.0456	1.182	1.2872	1.3789	1.4761	1.5958
1.5	0.8378	0.9961	1.1192	1.2174	1.3052	1.3933
2	0.5237	0.672	0.808	0.9266	1.03	1.1178
2.5	0.3234	0.4417	0.5621	0.6781	0.788	0.8884
3	0.2275	0.3184	0.4154	0.5136	0.6117	0.706
3.5	0.1317	0.1951	0.2687	0.3491	0.4354	0.5236
4	0.102	0.1524	0.2119	0.2782	0.3504	0.4265
5	0.0425	0.0669	0.0982	0.1363	0.1803	0.2324
6	0.0225	0.0365	0.0547	0.0779	0.106	0.1395
7	0.0131	0.0211	0.0325	0.0469	0.0653	0.0871
8	0.0101	0.0158	0.0247	0.0358	0.0499	0.067
10	0.0041	0.0052	0.0091	0.0136	0.019	0.0268
15	0.00076112	0.0012872	0.002409	0.0030746	0.0044431	0.0062022
20	0.00024632	0.00041908	0.0006898	0.0010151	0.0014786	0.0020816
50	6.6244E-06	0.000011387	0.000018379	0.000028225	0.000041635	0.000059409
80	1.0425E-06	1.8006E-06	2.9203E-06	4.5067E-06	6.6813E-06	9.5822E-06
100	4.3523E-07	7.5371E-07	1.2256E-06	1.8966E-06	2.8192E-06	4.0541E-06
1000	7.8875E-11	1.4474E-10	2.4844E-10	4.0445E-10	6.3068E-10	9.4897E-10
1000000	3.9694E-20	7.8204E-20	1.426E-19	2.4468E-19	3.9979E-19	6.2746E-19
1000000000	4.0375E-29	7.9997E-29	1.468E-28	2.5368E-28	4.1774E-28	6.6127E-28
x\Z	Al	Si	P	S	Cl	Ar
0	13	14	15	16	17	18

0.005	12.992	13.993	14.993	15.994	16.994	17.994
0.01	12.974	13.975	14.976	15.978	16.979	17.98
0.015	12.945	13.946	14.949	15.952	16.954	17.957
0.02	12.903	13.905	14.909	15.914	16.919	17.924
0.025	12.849	13.852	14.859	15.866	16.874	17.881
0.03	12.785	13.788	14.798	15.808	16.819	17.829
0.04	12.628	13.631	14.646	15.664	16.682	17.699
0.05	12.439	13.439	14.458	15.483	16.51	17.535
0.07	11.984	12.966	13.989	15.027	16.07	17.114
0.09	11.481	12.423	13.433	14.474	15.528	16.588
0.1	11.225	12.139	13.135	14.172	15.229	16.295
0.125	10.61	11.432	12.371	13.378	14.425	15.494
0.15	10.054	10.769	11.623	12.574	13.587	14.689
0.175	9.5711	10.179	10.934	11.805	12.762	13.776
0.2	9.1552	9.6693	10.32	11.099	11.98	12.937
0.25	8.4606	8.8521	9.3268	9.9162	10.621	11.428
0.3	7.8674	8.2232	8.5909	9.0285	9.5646	10.204
0.4	6.7617	7.1977	7.5406	7.8477	8.1686	8.5424
0.5	5.6864	6.2324	6.6672	7.0114	7.2976	7.5635
0.6	4.7049	5.3031	5.8182	6.2418	6.5848	6.8649
0.7	3.8742	4.461	5.0079	5.4892	5.8982	6.2366
0.8	3.2115	3.7411	4.2732	4.7754	5.2273	5.6196
0.9	2.7041	3.1541	3.6377	4.1262	4.5915	5.0165
1	2.3248	2.6922	3.11	3.5583	4.0097	4.4433
1.25	1.7537	1.9595	2.216	2.52	2.8628	3.2318
1.5	1.4812	1.5925	1.7379	1.928	2.1551	2.417
2	1.1924	1.2604	1.3287	1.4044	1.4941	1.6034
2.5	0.9755	1.0513	1.1174	1.1769	1.234	1.2929
3	0.7931	0.8725	0.9445	1.0101	1.0711	1.1298
3.5	0.6107	0.6936	0.7717	0.8433	0.9082	0.9668
4	0.5025	0.5774	0.65	0.7181	0.7816	0.8409

5	0.286	0.345	0.4065	0.4678	0.5283	0.589
6	0.1766	0.2189	0.2638	0.3098	0.3614	0.4125
7	0.113	0.1416	0.1741	0.2098	0.2468	0.2783
8	0.087	0.1096	0.1354	0.1641	0.1936	0.2268
10	0.0349	0.0456	0.0579	0.726	0.0873	0.1057
15	0.0084081	0.01116	0.01438	0.01825	0.02774	0.027995
20	0.0028477	0.0038011	0.0049671	0.006371	0.0080384	0.0099948
50	0.000082435	0.0001169	0.00014826	0.00019331	0.00024812	0.00031404
80	0.000013365	0.000018205	0.000024296	0.000031852	0.000041111	0.00005233
100	5.6698E-06	7.7437E-06	0.000010362	0.000013622	0.000017629	0.00022502
1000	1.3856E-09	1.9718E-09	2.7444E-09	3.7466E-09	5.0284E-09	6.6477E-09
1000000	9.523E-19	1.4048E-18	2.0226E-18	2.8515E-18	3.9472E-18	5.3767E-18
1000000000	1.013E-27	1.5094E-27	2.1966E-27	3.1327E-27	4.3899E-27	6.058E-27
x\Z	K	Ca	Sr	Ti	V	Cr
0	19	20	21	22	23	24
0.005	18.989	19.988	20.987	21.986	22.985	23.985
0.01	18.961	19.957	20.958	21.959	22.959	23.964
0.015	18.916	19.907	20.913	21.918	22.922	23.934
0.02	18.853	19.837	20.846	21.855	22.862	23.884
0.025	18.774	19.748	20.762	21.775	22.786	23.82
0.03	18.681	19.643	20.662	21.68	22.695	23.744
0.04	18.459	19.388	20.418	21.447	22.473	23.555
0.05	18.202	19.088	20.13	21.171	22.208	23.331
0.07	17.625	18.398	19.446	20.501	21.557	22.765
0.09	17.026	17.675	18.712	19.769	20.833	22.121
0.1	16.726	17.319	18.341	19.395	20.46	21.78

0.125	15.983	16.483	17.458	18.485	19.535	20.902
0.15	15.237	15.714	16.632	17.618	18.693	20.005
0.175	14.477	14.99	15.859	16.806	17.798	19.126
0.2	13.715	14.293	15.125	16.035	16.993	18.254
0.25	12.254	12.947	13.716	14.555	15.447	16.546
0.3	10.963	11.689	12.402	13.174	14.001	14.943
0.4	9.0418	9.6295	10.206	10.829	11.503	12.196
0.5	7.872	8.2524	8.6621	9.1224	9.634	10.153
0.6	7.1166	7.3767	7.6596	7.9786	8.3415	8.7237
0.7	6.5109	6.7498	6.9801	7.2173	7.4767	7.7569
0.8	5.9399	6.2095	6.4429	6.6571	6.8683	7.0886
0.9	5.3789	5.6909	5.9516	6.1785	6.3834	6.5814
1	4.8343	5.1814	5.4734	5.7254	5.946	6.1459
1.25	3.61	3.9821	4.3195	4.6267	4.902	5.1422
1.5	2.6907	3.002	3.3155	3.6237	3.9191	4.1894
2	1.7353	1.8918	2.0692	2.2651	2.4755	2.6915
2.5	1.3577	1.4319	1.5185	1.619	1.734	1.8618
3	1.1889	1.2501	1.3165	1.3893	1.4691	1.5562
3.5	1.0201	1.0684	1.1145	1.1596	1.2042	1.2507
4	0.8961	0.9473	0.9958	1.0424	1.0879	1.1336
5	0.6482	0.7051	0.7585	0.808	0.8554	0.8994
6	0.4613	0.5145	0.5667	0.6152	0.6618	0.7086
7	0.3296	0.3722	0.4156	0.4603	0.5051	0.5476
8	0.2614	0.2972	0.3338	0.3712	0.4099	0.4473
10	0.1251	0.1472	0.1703	0.1931	0.2195	0.2466
15	0.033951	0.040674	0.048192	0.056526	0.065692	0.075698
20	0.012265	0.014874	0.017845	0.021201	0.024962	0.02915
50	0.0003925 7	0.00048526	0.00059379	0.00071996	0.00086565	0.0010329
80	0.0000657 94	0.00008180 9	0.00010071	0.00012285	0.00014863	0.00017847

100	0.000028369	0.000035372	0.000043665	0.000053415	0.000064806	0.000078034
1000	8.671E-09	1.1174E-08	1.4245E-08	1.798E-08	2.2492E-08	2.7906E-08
1000000	7.2206E-18	9.5751E-18	1.2555E-17	1.6297E-17	2.0962E-17	2.67E-17
1000000000	8.2482E-27	1.1098E-26	1.4775E-26	1.9489E-26	2.5492E-26	3.3097E-26
x\Z	Mn	Fe	Co	Ni	Cu	Zn
0	25	26	27	28	29	30
0.005	24.984	25.983	26.983	27.984	28.984	29.984
0.01	24.961	25.961	26.962	27.963	28.967	29.965
0.015	24.929	25.932	26.935	27.938	28.947	29.942
0.02	24.875	25.88	26.885	27.89	28.906	29.898
0.025	24.806	25.814	26.822	27.829	28.854	29.841
0.03	24.723	25.735	26.745	27.755	28.791	29.773
0.04	24.518	25.538	26.556	27.573	28.635	29.603
0.05	24.274	25.302	26.329	27.353	28.448	29.397
0.07	23.66	24.707	25.751	26.793	27.962	28.868
0.09	22.962	24.023	25.082	26.139	27.387	28.244
0.1	22.598	23.666	24.732	25.795	27.081	27.914
0.125	21.665	22.736	23.808	24.88	26.243	27.019
0.15	20.739	21.803	22.874	23.946	25.536	26.095
0.175	19.858	20.911	21.972	23.039	24.461	25.184
0.2	19	20.033	21.079	22.135	23.538	24.266
0.25	17.348	18.34	19.352	20.38	21.688	22.471
0.3	15.768	16.729	17.698	18.689	19.869	20.72
0.4	12.997	13.809	14.659	15.524	16.481	17.392
0.5	10.809	11.468	12.172	12.918	13.667	14.519
0.6	9.2101	9.7165	10.27	10.868	11.464	12.189
0.7	8.0983	8.4697	8.8843	9.3425	9.8091	10.387

0.8	7.3331	7.6042	7.9086	8.2495	8.6078	9.0496
0.9	6.7782	6.9889	7.2189	7.4741	7.7492	8.0754
1	6.3312	6.515	6.7043	6.906	7.1235	7.3684
1.25	5.364	5.5586	5.7358	5.9013	6.0619	6.2194
1.5	4.4526	4.6866	4.899	5.0914	5.2648	5.4277
2	2.922	3.1488	3.3726	3.5901	3.7933	3.9972
2.5	2.0055	2.1594	2.3226	2.4929	2.6641	2.8448
3	1.6531	1.7578	1.8698	1.9882	2.1103	2.2412
3.5	1.3007	1.3562	1.417	1.4835	1.5566	1.6376
4	1.1806	1.2304	1.2831	1.3391	1.3989	1.4639
5	0.9404	0.9789	1.0154	1.0502	1.0834	1.1165
6	0.7535	0.7953	0.8353	0.8724	0.907	0.9408
7	0.5903	0.6317	0.6731	0.7138	0.7498	0.7837
8	0.4847	0.5227	0.5593	0.5972	0.6308	0.6639
10	0.2736	0.3048	0.3317	0.3641	0.3929	0.4242
15	0.086549	0.098241	0.11077	0.12411	0.13927	0.1532
20	0.033781	0.038874	0.0044441	0.050496	0.057051	0.064113
50	0.0012237	0.0014403	0.0016851	0.0019605	0.0022689	0.0026131
80	0.0002128	0.00025212	0.00029693	0.00034779	0.00040527	0.00047001
100	0.000093312	0.00011087	0.00013096	0.00015384	0.00017979	0.00020913
1000	3.4365E-08	4.2027E-08	5.1071E-08	6.1696E-08	7.4126E-08	8.861E-08
1000000	3.3862E-17	4.2589E-17	5.3236E-17	6.6171E-17	8.1828E-17	1.0072E-16
1000000000	4.2685E-26	5.4722E-26	6.9775E-26	8.854E-26	1.1186E-25	1.4078E-25
x\Z	Ga	Ge	As	Se	Br	Kr
0	31	32	33	34	35	36
0.005	30.979	31.983	32.986	33.988	34.99	35.99

0.01	30.957	31.96	32.963	33.966	34.967	35.969
0.015	30.932	31.931	32.931	33.932	34.933	35.935
0.02	30.881	31.877	32.877	33.879	34.881	25.884
0.025	30.815	31.809	32.809	33.811	34.815	35.819
0.03	30.735	31.727	32.726	33.73	34.735	35.741
0.04	30.539	31.522	32.521	33.526	34.534	35.544
0.05	30.306	31.275	32.268	33.272	34.283	35.297
0.07	29.706	30.645	31.625	32.628	33.642	34.663
0.09	29.016	29.907	30.859	31.847	32.856	33.878
0.1	28.657	29.519	30.45	31.424	32.425	33.444
0.125	27.703	28.491	29.361	30.29	31.26	32.26
0.15	26.74	27.46	28.26	29.127	30.047	31.009
0.175	25.819	26.478	27.201	27.993	28.846	29.752
0.2	24.907	25.527	26.187	26.908	27.69	28.53
0.25	23.157	23.761	24.346	24.953	25.601	26.3
0.3	21.473	22.118	22.695	23.249	23.808	24.394
0.4	18.246	19.014	19.691	20.289	20.829	21.334
0.5	15.374	16.192	16.951	17.642	18.262	18.82
0.6	12.951	13.723	14.485	15.216	15.902	16.535
0.7	11.011	11.679	12.374	13.075	13.765	14.43
0.8	9.5351	10.077	10.663	11.281	11.918	12.558
0.9	8.4473	8.8673	9.3346	9.8452	10.391	10.963
1	7.6499	7.9681	8.3277	8.7306	9.1754	9.6573
1.25	6.3821	6.5559	6.747	6.9608	7.2023	7.475
1.5	5.5837	5.7274	5.8649	6.0025	6.1467	6.3025
2	4.1907	4.3732	4.5438	4.7024	4.8492	4.9853
2.5	3.0276	3.2108	3.3924	3.5702	3.7426	3.9082
3	2.3774	2.5178	2.6608	2.8054	2.9508	3.0959
3.5	1.7272	1.8247	1.9292	2.0407	2.1591	2.2936
4	1.5348	1.6112	1.6926	1.7793	1.8714	1.9688
5	1.15	1.1843	1.2195	1.2564	1.2961	1.3391

6	0.9733	1.0039	1.033	1.0618	1.0902	1.1182
7	0.8182	0.8526	0.886	0.9161	0.9418	0.9662
8	0.6969	0.7307	0.7629	0.793	0.8202	0.846
10	0.4542	0.4868	0.5166	0.5468	0.5769	0.6057
15	0.16889	0.1853	0.20242	0.22019	0.23858	0.25757
20	0.07169	0.079786	0.088404	0.097545	0.10721	0.11739
50	0.0029958	0.0034198	0.003888	0.0044035	0.0049695	0.0055892
80	0.0005426 6	0.00062392	0.00071454	0.0008153	0.00092702	0.0010506
100	0.0002421 9	0.0002793	0.00032084	0.00036722	0.00041884	0.00047617
1000	1.0543E-07	1.2488E-07	1.4732E-07	1.7312E-07	2.0271E-07	2.3655E-07
1000000	1.2343E-16	1.5066E-16	1.8324E-16	2.2213E-16	2.6843E-16	3.2348E-16
1000000000	1.7654E-25	2.2069E-25	2.7511E-25	3.4207E-25	4.2437E-25	5.2541E-25
x\Z	Rb	Sr	Y	Zr	Nb	Mo
0	37	38	39	40	41	42
0.005	36.973	37.972	38.976	39.982	40.985	41.986
0.01	36.938	37.932	38.937	39.944	40.951	41.954
0.015	36.889	37.876	38.88	39.884	40.899	41.902
0.02	36.805	37.781	38.788	39.796	40.821	41.827
0.025	36.699	37.662	38.672	39.683	40.722	41.732
0.03	36.575	37.521	38.534	39.549	40.604	41.618
0.04	36.278	37.18	38.198	39.221	40.312	41.335
0.05	35.948	36.793	37.807	38.831	39.96	40.991
0.07	35.146	35.862	36.858	37.889	39.095	40.141
0.09	34.306	34.894	35.84	36.849	38.104	39.155
0.1	33.861	34.406	35.322	36.313	37.578	38.627

0.125	32.775	33.247	34.069	34.995	36.238	37.267
0.15	31.632	32.113	32.859	33.719	34.887	35.879
0.175	30.474	31.022	31.708	32.496	33.557	34.502
0.2	29.327	29.942	30.594	31.322	32.266	33.156
0.25	27.079	27.794	28.421	29.078	29.815	30.599
0.3	25.079	25.797	26.399	27.008	27.604	28.288
0.4	21.862	22.438	22.99	23.518	23.98	24.506
0.5	19.346	19.839	20.338	20.808	21.242	21.682
0.6	17.112	17.636	18.134	18.614	19.072	19.494
0.7	15.044	15.624	16.167	16.688	17.178	17.637
0.8	13.174	13.776	14.358	14.911	15.422	15.932
0.9	11.546	12.125	12.709	13.265	13.811	14.329
1	10.174	10.699	11.242	11.778	12.313	12.837
1.25	7.7817	8.122	8.4922	8.8899	9.3098	9.7497
1.5	6.4893	6.6766	6.9156	7.1491	7.4077	7.694
2	5.1121	5.2316	5.3463	5.4599	5.5763	5.6982
2.5	4.0652	4.2129	4.2129	4.4766	4.5937	4.7043
3	3.2392	3.3794	3.5145	3.6453	3.77	3.8911
3.5	2.4132	2.5459	2.6796	2.8139	2.9463	3.078
4	2.0706	2.1758	2.2827	2.3913	2.5001	2.61
5	1.3853	1.4355	1.489	1.5461	1.6078	1.674
6	1.1464	1.175	1.206	1.2386	1.2728	1.3093
7	0.9922	1.0188	1.045	1.0701	1.0953	1.1206
8	0.8733	0.9008	0.9271	0.9528	0.9779	1.0029
10	0.6356	0.6647	0.6914	0.7175	0.7431	0.7675
15	0.2771	0.29713	0.31763	0.33856	0.35986	0.38152
20	0.12809	0.13929	0.15099	0.16319	0.17586	0.18901
50	0.0062659	0.0070031	0.0078042	0.008673	0.0096131	0.010628
80	0.0011869	0.001337	0.0015019	0.0016826	0.0018802	0.0020961
100	0.0005396 7	0.00060987	0.00068728	0.00077249	0.0008661	0.00096875

1000	2.7517E-07	3.1914E-07	3.6908E-07	4.2572E-07	4.8981E-07	5.6221E-07
1000000	3.881E-16	4.6621E-16	5.5781E-16	6.6606E-16	7.9386E-16	9.4459E-16
1000000000	6.4936E-25	8.013E-25	9.8745E-25	1.2154E-24	1.4945E-24	1.8362E-24
x\Z	Tc	Ru	Rh	Pd	Ag	Cd
0	43	44	45	46	47	48
0.005	42.985	43.987	44.987	45.992	46.987	47.986
0.01	42.951	43.957	44.958	45.969	46.959	47.956
0.015	42.896	43.909	44.912	45.93	46.917	47.91
0.02	42.816	43.839	44.844	45.875	46.852	47.841
0.025	42.714	43.749	44.757	45.805	46.77	47.753
0.03	42.592	43.642	44.652	45.72	46.672	47.647
0.04	42.291	43.375	44.393	45.507	46.425	47.383
0.05	41.924	43.048	44.075	45.238	46.123	47.059
0.07	41.022	42.232	43.275	44.545	45.356	46.239
0.09	39.982	41.267	42.324	43.675	44.435	45.263
0.1	39.43	40.744	41.806	43.185	43.93	44.733
0.125	38.023	39.371	40.436	41.838	42.576	43.329
0.15	36.613	37.94	38.995	40.366	41.131	41.859
0.175	35.234	36.497	37.53	38.829	39.643	40.376
0.2	33.897	35.066	36.069	37.274	38.137	38.89
0.25	31.353	32.308	33.224	34.239	35.153	35.964
0.3	29.024	29.786	30.599	31.444	32.341	33.184
0.4	25.12	25.633	26.244	26.836	27.576	28.343
0.5	22.161	22.567	23.029	23.472	24.019	24.619
0.6	19.904	20.284	20.666	21.036	21.44	21.883
0.7	18.047	18.447	18.815	19.169	19.509	19.857
0.8	16.377	16.816	17.212	17.589	17.927	18.249
0.9	14.81	15.285	15.72	16.134	16.504	16.845

1	13.339	13.834	14.3	14.747	15.156	15.533
1.25	10.204	10.665	11.129	11.591	12.045	12.484
1.5	8.0082	8.3463	8.7069	9.0843	9.479	9.883
2	5.8283	5.9707	6.1262	6.2974	6.4852	6.6907
2.5	4.8096	4.9087	5.0061	5.1029	5.2013	5.3031
3	4.0091	4.1209	4.2306	4.3373	4.4433	4.5486
3.5	3.2087	3.3332	3.4552	3.5716	3.6852	3.7941
4	2.7206	2.8281	2.9352	3.0394	3.143	3.2442
5	1.7445	1.818	1.8953	1.9751	2.0585	2.1445
6	1.3475	1.3882	1.4324	1.4788	1.5278	1.5803
7	1.146	1.1715	1.1975	1.2248	1.2543	1.2859
8	1.0279	1.0531	1.0784	1.1038	1.1303	1.158
10	0.7917	0.8164	0.8401	0.8618	0.8822	0.9021
15	0.40348	0.4257	0.44815	0.4708	0.4936	0.51653
20	0.2026	0.21664	0.2311	0.24597	0.26123	0.27687
50	0.011722	0.012899	0.014163	0.015518	0.016968	0.018518
80	0.0023313	0.0025872	0.0028652	0.0031668	0.0034933	0.0038464
100	0.0010811	0.0012039	0.0013378	0.0014838	0.0016425	0.001815
1000	6.4388E-07	7.3585E-07	8.3927E-07	9.554E-07	1.0857E-06	1.2316E-06
1000000	1.1222E-15	1.3314E-15	1.5775E-15	1.867E-15	2.2074E-15	2.6074E-15
1000000000	2.2544E-24	2.7664E-24	3.39E-24	4.16E-24	5.1019E-24	6.2552E-24
x\Z	In	Sn	Sb	Te	I	Xe
0	49	50	51	52	53	54
0.005	48.98	49.981	50.983	51.985	52.986	53.988
0.01	48.947	49.946	50.948	51.95	52.952	53.953
0.015	48.899	49.895	50.894	51.894	52.895	53.897
0.02	48.821	49.814	50.812	51.813	52.814	53.817

0.025	48.722	49.712	50.708	51.709	52.711	53.714
0.03	48.803	49.588	50.583	51.583	52.586	53.591
0.04	48.308	49.28	50.27	51.269	52.273	53.28
0.05	47.952	48.906	49.886	50.881	51.884	52.892
0.07	47.054	47.964	48.92	49.902	50.9	51.909
0.09	46.01	46.862	47.775	48.728	49.707	50.706
0.1	45.453	46.274	47.161	48.093	49.057	50.044
0.125	44	44.743	45.555	46.423	47.335	48.282
0.15	42.51	43.192	43.93	44.724	45.568	46.455
0.175	41.037	41.683	42.357	43.075	43.842	44.655
0.2	39.579	40.212	40.843	41.5	42.195	42.934
0.25	36.719	37.388	38.005	38.601	39.199	39.814
0.3	33.989	34.719	35.378	35.983	36.555	37.11
0.4	29.126	29.894	30.628	31.314	31.95	32.538
0.5	25.26	25.932	26.619	27.304	27.973	28.615
0.6	22.36	22.881	23.44	24.029	24.636	25.25
0.7	20.22	20.611	21.036	21.496	21.99	22.511
0.8	18.565	18.885	19.218	19.574	19.956	20.368
0.9	17.165	17.469	17.766	18.065	18.374	18.7
1	15.882	16.205	16.507	16.795	17.076	17.357
1.25	12.905	13.304	13.678	14.028	14.354	14.658
1.5	10.292	10.699	11.1	11.491	11.867	12.227
2	6.9144	7.156	7.4147	7.6893	7.9779	8.2785
2.5	5.4102	5.5243	5.6471	5.7801	5.9245	6.0813
3	4.6541	4.7606	4.8691	4.9804	5.0953	5.2147
3.5	3.8979	3.9969	4.0911	4.1807	4.2662	4.3481
4	3.3429	3.4392	3.5329	3.6239	3.7244	3.7985
5	2.233	2.3238	2.4165	2.5104	2.6408	2.6992
6	1.6352	1.6924	1.7531	1.8172	1.8841	1.9537
7	1.3196	1.3552	1.3922	1.4309	1.4721	1.5161
8	1.187	1.217	1.2478	1.2799	1.3138	1.3495

10	0.9218	0.9407	0.9591	0.9779	0.9973	1.0168
15	0.53954	0.56262	0.58573	0.60884	0.63193	0.65497
20	0.29287	0.30921	0.32587	0.34283	0.36008	0.37759
50	0.020171	0.021932	0.023805	0.025795	0.027907	0.030144
80	0.0042277	0.0046388	0.0050817	0.0055581	0.0060699	0.0066192
100	0.002002	0.0022047	0.002424	0.00026611	0.002917	0.003193
1000	1.3948E-06	1.5773E-06	1.7811E-06	2.0084E-06	2.2617E-06	2.5438E-06
1000000	3.0773E-15	3.6293E-15	4.2776E-15	5.0389E-15	5.933E-15	6.9831E-15
1000000000	7.6697E-24	9.4057E-24	1.1538E-23	1.4159E-23	1.7383E-23	2.1353E-23

x\Z	Cs	Ba	La	Ce	Pr	Nd
0	55	56	57	58	59	60
0.005	54.971	55.97	56.964	57.963	58.968	59.967
0.01	54.92	55.912	56.909	57.909	58.914	59.914
0.015	54.84	55.823	56.827	57.831	58.834	59.837
0.02	54.72	55.688	56.695	57.702	58.707	59.713
0.025	54.57	55.519	56.53	57.54	58.549	59.557
0.03	54.393	55.32	56.333	57.346	58.36	59.372
0.04	53.97	54.841	55.856	56.878	57.906	58.926
0.05	53.491	54.292	55.309	56.342	57.386	58.415
0.07	52.361	53.013	53.989	55.036	56.144	57.186
0.09	51.147	51.679	52.587	53.645	54.832	55.885
0.1	50.499	51	51.867	52.929	54.157	55.213
0.125	48.874	49.375	50.125	51.188	52.509	53.57
0.15	47.172	47.715	48.4	49.454	50.841	51.9
0.175	45.434	46.068	46.717	47.763	49.168	50.225
0.2	43.741	44.439	45.074	46.103	47.493	48.542
0.25	40.542	41.277	41.887	42.862	44.169	45.18

0.3	37.727	38.407	38.997	39.9	41.087	42.039
0.4	33.099	33.652	34.207	34.951	35.882	36.691
0.5	29.218	29.755	30.345	30.981	31.703	32.395
0.6	25.849	26.431	27.01	27.573	28.144	28.749
0.7	23.043	23.59	24.133	24.626	25.088	25.614
0.8	20.806	21.269	21.74	22.163	22.543	22.991
0.9	19.051	19.424	19.812	20.169	20.491	20.866
1	17.651	17.954	18.273	18.576	18.858	19.171
1.25	14.941	15.21	15.469	15.714	15.95	16.184
1.5	12.574	12.894	13.202	13.483	13.741	13.992
2	8.5886	8.9052	9.2253	9.5267	9.8083	10.1
2.5	6.2508	6.4336	6.6302	6.8321	7.0355	7.2521
3	5.3389	5.4686	5.6045	5.7439	5.8854	6.0336
3.5	4.4271	4.5036	4.5788	4.6557	4.7353	4.8151
4	3.8823	3.9642	4.0446	4.1253	4.2071	4.2886
5	2.7926	2.8854	2.9761	3.0644	3.1506	3.2357
6	2.0251	2.099	2.1731	2.2471	2.3221	2.3991
7	1.5626	1.6106	1.6608	1.7128	1.7656	1.8203
8	1.3864	1.4241	1.4633	1.5038	1.545	1.5874
10	1.0339	1.0512	1.0683	1.0858	1.1037	1.1217
15	0.67795	0.70083	0.7236	0.74625	0.76875	0.79109
20	0.39535	0.41335	0.43155	0.44995	0.46852	0.48726
50	0.032511	0.033014	0.037656	0.040442	0.043377	0.046466
80	0.0072081	0.0078387	0.0085133	0.0092343	0.010004	0.010825
100	0.0034903	0.0038103	0.0041543	0.0045238	0.0049204	0.0053457
1000	2.8577E-06	3.2068E-06	3.5947E-06	4.0254E-06	4.5034E-06	5.0337E-06
1000000	8.2165E-15	9.6656E-15	1.1368E-14	1.337E-14	1.5723E-14	1.8492E-14
1000000000	2.6247E-23	2.9E-23	3.9747E-23	4.90E-23	6.0404E-23	7.4577E-23

Appendix C

Photoelectric cross-section calculation – code:

```
function sigma_ph = F_E(E,Z_eff)
E = E*1.602176565*10^(-19); %energy in jouls
m_e = 9.109534*10^-31; %rest mass of the electron -
Hubbel paper
%m_e = 511003.4; %mass in eV/c2
e_charge = 1.51891014*10^-14; %electron charge

h_bar = 1.0545718*10^-34; %Dirac constant in J*s
c = 2.99792458*10^8; %speed of light in meters
load N_z.mat



alpha = (e_charge^2)/(h_bar*c); %fine structure by Hubbel
paper

e_k = (Z_eff^2)*(alpha^2)*m_e*(c^2)/2;

n_1 = (e_k/(E - e_k))^0.5;
f_n_1 = exp(-4*n_1*acot(n_1))/(1-exp(-2*pi*n_1));
S_E_Z = 2*pi*((e_k/E)^0.5)*f_n_1;
```

```
beta = sqrt(2*E/(m_e*c^2));


f_b_term = 1 + 0.143*beta^2 + 1.667*beta^8;

N_Z_term = interp1(N_z(:,1),N_z(:,2),Z_eff,'pchip');

thompson_cross = (8*pi/3)*((e_charge^2)/(m_e*c^2))^2;
alpha = (e_charge^2)/(h_bar*c); %fine structure by Hubbel
paper
sigma_BA =
4*sqrt(2)*(alpha^4)*(((m_e*c^2)/E)^(7/2))*thompson_cross;

sigma_ph = sigma_BA*S_E_Z*N_Z_term*f_b_term;
```

Scattering cross-section calculation – code:

```
function sigma_scat = G_E(E,Z_eff)

k = E/511003.4; %in eV
r_e = 2.8179380*10^(-15); % electron radius
m_e = 9.109534*10^-31; %rest mass of the electron -
Hubbel paper
e_charge = 1.5189186*10^-14; %for alpha, apparently use
third one in Hubbel paper
h = 2*pi*1.0545718*10^-34; %Planck's constant in J*s
c = 2.99792458*10^8; %speed of light in meters
Z_shtrih = 35;
```

```
b_parameter = 0.35; %for higher Z better use b = 0.3
(Tin), or b = 0.35 (Copper), or 0.42 (Aluminum)

thompson_cross = (8*pi/3)*((e_charge^2)/(m_e*c^2))^2;
%thompson_cross = 6.65242873*10^(-29);



x = [-1:0.001:1];
e_shtrih = ((Z_shtrih/Z_eff)^(1/3))*E;
y = i_f(x,e_shtrih,Z_shtrih, Z_eff);
integral_part = trapz(x,y);

sigma_coh = (1-Z_eff^(b_parameter-
1))*(Z_eff/Z_shtrih^2)*(3/8)*thompson_cross*integral_part
;



sigma_KN = 2*pi*(r_e^2)*(((1+k)/k^2)*((2*(1+k)/(1+2*k))-
((log(1+2*k))/k)) + (log(1+2*k))/(2*k) -
(1+3*k)/((1+2*k)^2));

sigma_scat = (sigma_KN + sigma_coh);


function int_fun = i_f(theta_c, E, Z_shtrih, Z_eff)

k = E/511003.4; %in eV
r_e = 2.8179380*10^(-15); % electron radius
```

```
m_e = 9.109534*10^-31; %rest mass of the electron -
Hubbel paper
e_charge = 1.5189186*10^-14; %for alpha, apparently use
third one in Hubbel paper
h = 2*pi*1.0545718*10^-34; %Planck's constant in J*s
c = 2.99792458*10^8; %speed of light in meters

load Fx.mat
load xmoments.mat
b = [1:60];
[X,Y] = meshgrid(b,a);

lambda = 12398.520/(E);
xm = sqrt((1-theta_c)/2)./lambda;

int_fun =
((1+theta_c.^2)').*((interp2(X,Y,V,Z_shtrih,xm)).^2);
```